AI Identifies Broadly Neutralizing Antibodies from an IGHV1-69 Public Antibody Class Exerting Continued Selection Over SARS-CoV-2

Chuanying Niu[1,2,†], Xiaohan Huang[3,†], Qihong Yan[3,†], Banghui Liu[2,4,†], Xijie Gao[5,†], Yidong Song[6,†], Jingjing Wang[2], Longyu Wang[7,8], Zimu Li[7,8], Huiran Zheng[3], Ping He[7], Xiaodong Huang[7,8], Hang Yuan[2], Binqian Zou[2,8], Yuedong Yang[6], Fandi Wu[9], Yicheng Yao[10], Gul Habib[2], Xinwen Chen[7], Ling Chen[7,*], Jun He[2,*], Jianhua Yao[9,*], Jincun Zhao[3,*], Xiaoli Xiong[2,*]

[1]Division of Life Sciences and Medicine, University of Science and Technology of China, Hefei 230026, China.
[2]State Key Laboratory of Respiratory Disease, Guangdong Provincial Key Laboratory of Stem Cell and Regenerative Medicine, Guangdong-Hong Kong Joint Laboratory for Stem Cell and Regenerative Medicine, Guangzhou Institutes of Biomedicine and Health, Chinese Academy of Sciences, Guangzhou 510530, China.
[3]State Key Laboratory of Respiratory Disease, National Clinical Research Center for Respiratory Disease, Guangzhou Institute of Respiratory Health, the First Affiliated Hospital of Guangzhou Medical University, Guangzhou, China.
[4]Institute of Urban Agriculture, Chinese Academy of Agricultural Sciences, Chengdu 610213, China.
[5]Key Laboratory of Biological Targeting Diagnosis, Therapy and Rehabilitation of Guangdong Higher Education Institutes, The Fifth Affiliated Hospital of Guangzhou Medical University, Guangzhou 510799, China
[6]School of Computer Science and Engineering, Sun Yat-sen University, Guangzhou, Guangdong, China.
[7]Guangzhou National Laboratory, Guangzhou 510005, China.
[8]Guangzhou Medical University, Guangzhou, 511436, China.
[9]Tencent, AI for Life Sciences Lab, Shenzhen, China.
[10]School of Life Sciences, Sun Yat-sen University, Guangzhou, China.
†These authors contributed equally to this work.
*Corresponding author. Email: chen_ling@gibh.ac.cn (L.C.); he_jun@gibh.ac.cn (J.H.); jianhua.yao@gmail.com (J.Y.); zhaojincun@gird.cn (J.Z.); xiong_xiaoli@gibh.ac.cn (X.X.)

Abstract

R1-32-like public antibodies, characterized by shared IGHV1-69/IGLV1-40 usage and non-ACE2-competing, spike-destroying activity, are elicited in more than 50% of individuals with COVID-19 and have been implicated in driving recurrent mutations at $L452_{SARS2}$ and $F490_{SARS2}$ within their convergent epitope in the SARS-CoV-2 spike receptor-binding domain. These mutations effectively mediate escape from non-affinity-matured R1-32-like antibodies with germline-like sequences. Here, we characterize four affinity-matured R1-32-like antibodies, C092, C807, BD56-104, and BD56-597, with the ability to tolerate $L452_{SARS2}$ and $F490_{SARS2}$ mutations. We show that this tolerance arises from residues introduced by somatic hypermutation at convergent positions across multiple CDR loops and surrounding regions, thereby creating additional contacts that reinforce epitope binding. An unusual $N354_{SARS2}$ glycosylation site, which emerged in BA.2.86 and became fixed in its descendants, is linked to escape from affinity-matured R1-32-like antibodies, implying ongoing selection by this public antibody class. Using an AI model trained on integrated structural, neutralization, and binding data, we further identified ZL525, an ultrapotent R1-32-like antibody with pan-SARS-CoV-2 variant activity, including against the highly evasive KP.3 variant carrying the $N354_{SARS2}$ glycosylation, and broad sarbecovirus cross-reactivity extending to SARS-CoV-1. Together, these findings highlight how public antibodies shape SARS-CoV-2 antigenic evolution and demonstrate the power of AI-empowered strategies for discovering broadly neutralizing antibodies.

54 **Introduction**

55 The ongoing evolution of SARS-CoV-2, driven by immune pressure established from natural
56 infections and vaccinations, has led to extensive amino acid substitutions in the spike (S)
57 protein, the major viral surface glycoprotein and principal target of neutralizing antibodies (*1-*
58 *3*). Several key residues in the receptor-binding domain (RBD), such as K417$_{SARS2}$,
59 L452$_{SARS2}$, E484$_{SARS2}$, F490$_{SARS2}$, and N501$_{SARS2}$, have become recurrent mutation hotspots
60 across variants, enhancing immune evasion and viral fitness (*1, 4-8*).
61
62 Based on their epitope locations, specifically whether they compete with ACE2 binding or
63 require the RBD to adopt an 'up' conformation, SARS-CoV-2 RBD-targeting antibodies have
64 been broadly classified into four epitope classes (*9*). In addition, many RBD-targeting
65 antibodies isolated early in the pandemic exhibit germline-like sequences with low levels of
66 somatic hypermutation (*10-12*). Some of these antibodies can be further grouped into distinct
67 public (population) antibody classes, defined by convergent epitope recognition and shared
68 genetic origins (*13-15*). Such population-level responses are thought to impose strong
69 selective pressure on the virus and provide valuable insights into SARS-CoV-2 antigenic drift
70 (*16-18*).
71
72 For example, many IGHV3-53/3-66-encoded public antibodies, which target the ACE2-
73 binding site and are classified as epitope class 1, were effectively abrogated by the K417$_{SARS2}$
74 mutation (*9, 19, 20*). Many IGHV1-2-encoded public antibodies, which recognize RBD in
75 both 'up' and 'down' conformations and are classified as epitope class 2, are strongly evaded
76 by E484$_{SARS2}$ substitutions (*21, 22*). Notably, we identified a public antibody class defined by
77 the use of the IGLV6-57 light chain gene, which pairs with heavy chains of diverse genetic
78 origins (*14*). These antibodies target a class 4 epitope relatively conserved among
79 sarbecoviruses, encompassing RBD residues S371-S373-S375$_{SARS2}$. Strikingly, we show that
80 the featured Omicron S371L/F-S373P-S375F$_{SARS2}$ mutations within this epitope mediate the
81 escape of many IGLV6-57-class public antibodies (*14*). Other public antibody classes,
82 including IGHV1-58/IGKV3-20 and IGHV2-5/IGLV2-14, display some breadth but remain
83 variably susceptible to escape by mutations at F486$_{SARS2}$ and positions 444-445$_{SARS2}$,
84 respectively (*23-26*).
85
86 We have also previously identified a class of R1-32-like public antibodies elicited in more
87 than 50% of COVID-19 convalescents early in the pandemic. These antibodies are
88 characterized by shared usage of the IGHV1-69/IGLV1-40 gene pairing and rely on the
89 unique features of the IGHV1-69 gene, whose germline-encoded hydrophobic HCDR2
90 residues bind the hydrophobic RBD residues L452$_{SARS2}$ and F490$_{SARS2}$. This specific
91 interaction renders them vulnerable to mutations at L452 and F490. (*16, 27*). These residues
92 have since emerged as mutation hot-spots for viral escape (*1, 16, 27*). While the Delta variant
93 harbored the L452R$_{SARS2}$ mutation, subsequent Omicron subvariants acquired

L452R/Q/M_{SARS2} or F490S_{SARS2} mutations across multiple lineages (e.g., BA.4/5, BF.7, BQ.1.1, XBB, EG.5), reflecting sustained immune pressure at these positions (*28-30*).

Intriguingly, we found that several members of the R1-32-like public antibody class, including C092, C807, BD56-104, and BD56-597, retain robust binding to S-proteins of viral variants carrying mutations at positions 452_{SARS2} and 490_{SARS2}. The mechanism by which these antibodies maintain cross-variant reactivity despite substitutions at key contact residues has remained unclear. In this study, we elucidate the structural and biochemical basis for their mutation tolerance. We show that somatic hypermutation introduced residues, following convergent patterns, confer resilience to antigenic epitope changes, including those located at $L452_{SARS2}$ and $F490_{SARS2}$, and resulting in broadened reactivity not only to SARS-CoV-2 variants but also to other SARS-related coronaviruses. Using our structural-functional relationship data, we trained an AI-based antibody discovery model (*31*), which led to the identification of ZL525, an elite R1-32-like antibody with ultrapotent, pan-variant neutralizing activity, capable of neutralizing the latest variants carrying a highly unusual epitope glycan mutation and extending cross-reactivity to SARS-CoV-1. Our findings illuminate the adaptability of public antibodies in response to the ongoing antigenic drift of SARS-CoV-2 and highlight the power of AI-driven approaches to identify broadly-neutralizing antibodies.

Results

Identification of R1-32-like public antibodies that tolerate spike mutations

We have previously defined IGHV1-69 encoded R1-32-like public antibodies as those that either exhibit a minimum of 80% amino acid similarity to R1-32 or FC08 in the HCDR3 region or contain a GYSGYG/D motif in HCDR3 (*16, 27*). In our previous study, we identified and characterized 10 R1-32-like antibodies isolated from ancestral (or wildtype, WT) SARS-CoV-2 convalescents or vaccinees (*27, 32-35*). Notably, among these, C092 and C807 showed no obvious reduction in binding to SARS-CoV-2 RBD variants with L452 or F490 mutations, including Delta (L452R_{SARS2}), Kappa (L452R_{SARS2}), and Lambda (L452Q_{SARS2}+F490S_{SARS2}) RBDs (*27*). We further identified BD56-104 and BD56-597 as mutation-resistant R1-32-like public antibodies that effectively neutralize Omicron subvariants BA.2.12.1 (L452Q_{SARS2}), BA.2.13 (L452M_{SARS2}), and BA.4/5 (L452R_{SARS2}), through the analysis of published sequence and neutralization data (*28*) (**Fig. S1a**). Notably, both BD56-104 and BD56-597 were isolated from convalescents with Omicron BA.1 breakthrough infections (*28*). In contrast to R1-32, which has minimal somatic hypermutation (SHM), the 4 mutation-resistant antibodies, C092, C807, BD56-104, and BD56-597, carry 6-15 SHMs in their heavy chains and 3-4 SHMs in their light chains, indicative of substantial affinity maturation (**Fig.1a and b**).

133 To further characterize these R1-32-like public antibodies, we performed antigen binding
134 assays for C092, C807, BD56-104, and BD56-597 against a more comprehensive and
135 updated panel of SARS-CoV-2 RBDs, which we classified into 4 categories: 1) RBDs with
136 single amino acid substitutions at key residues ($K417_{SARS2}$, $E484_{SARS2}$, $T478_{SARS2}$, $L452_{SARS2}$,
137 $F490_{SARS2}$); 2) RBDs from early VOC/VOI variants (Alpha to Lambda); 3) RBDs from early
138 Omicron variants (BA.1 to BA.4/5); and 4) RBDs from later-emerging Omicron subvariants,
139 including BQ, XBB, and EG variants. Within each category, mutants containing $L452_{SARS2}$
140 and $F490_{SARS2}$ mutations were further grouped together **(Fig. 1c and Fig. S1b-e)**.
141
142 The results showed that C092, C807, BD56-104, and BD56-597 retained high-affinity
143 binding (K_D < 1.2 nM) to SARS-CoV-2 RBDs carrying $L452_{SARS2}$ and $F490_{SARS2}$ single
144 mutations. In contrast, the germline-like R1-32 exhibited substantially reduced binding to
145 these mutant RBDs (K_D = 11.8-54.2 nM) **(Fig. 1c and Fig. S1b-e)**. Substitutions at
146 $K417_{SARS2}$, $E484_{SARS2}$, and $T478_{SARS2}$, commonly associated with the escape of epitope class
147 1 and class 2 antibodies (*9, 20, 21*), had minimal impact on the binding of C092, C807,
148 BD56-104, and BD56-597 **(Fig. 1c and Fig. S1b-e)**, consistent with these residues being
149 located at the periphery or outside of the epitope recognized by the R1-32 class of public
150 antibodies.
151
152 C092, C807, BD56-104, and BD56-597 maintained very high affinities (K_D < 0.3 nM)
153 towards RBDs of variants carrying no mutations at 452_{SARS2} or 490_{SARS2}, including Alpha
154 (B.1.1.7), Beta (B.1.351), Gamma (P.1), and multiple Omicron sublineages (BA.1, BA.1.1,
155 BA.2, BA.3, BA.2.75, and BA.2.75.2). Consistent with their mutation tolerance, C092, C807,
156 BD56-104, and BD56-597 also maintained high affinities (K_D < 2.1 nM) towards RBDs
157 harboring $L452_{SARS2}$ substitutions, including Kappa (B.1.617.1), Delta (B.1.617.2), Omicron
158 BA.2.11, BA.2.12.1, BA.2.13, BA.4/5, BF.7, and BQ.1.1. For comparison, germline-like R1-
159 32 exhibited substantially reduced binding to these mutants (K_D > 55 nM).
160
161 Notably, C092, C807, BD56-104, and BD56-597 maintained high affinities (K_D < 4.5 nM)
162 towards RBDs of the later emerged XBB lineages (XBB, XBB.1.5), and EG.5 lineages
163 (EG.5, EG.5.1), despite the presence of $F490S_{SARS2}$ mutations in these variants. All four
164 antibodies exhibited the weakest binding to the Lambda (C.37) RBD carrying both the
165 $L452_{SARS2}$ and $F490_{SARS2}$ mutations, although their K_D values are still below 6.8 nM **(Fig. 1c**
166 **and Fig. S1b-e)**. For comparison, the germline-like R1-32 binds Lambda RBD with a K_D of ~
167 1000 nM, representing a reduction of ~1000-fold.
168
169 These RBD binding results confirm that BD56-104 and BD56-597, like C092 and C807, are
170 tolerant to diverse variants carrying $L452_{SARS2}$ and $F490_{SARS2}$. Among them, we found that
171 C092 and BD56-597 consistently exhibited more robust binding across RBD variants
172 compared to C807 and BD56-104. C807 showed moderately but noticeably reduced binding

173 to RBDs harboring $L452_{SARS2}$ mutations, such as those in Kappa, Delta, Lambda, Omicron
174 BA.4/5, BF.7, and BQ.1.1, characterized by accelerated dissociation kinetics (**Fig. S1c**).
175 BD56-104 also showed moderate but noticeable sensitivity to $F490_{SARS2}$ substitutions,
176 displaying accelerated dissociation from RBDs of Lambda, XBB lineages (XBB, XBB.1.5),
177 and EG.5 lineages (EG.5, EG.5.1) that carry this mutation (**Fig. S1d**).
178

179 R1-32-like antibodies tolerate mutations and maintain neutralization

180 Neutralization activities of C092, C807, BD56-104, and BD56-597 were evaluated using
181 VSV-based pseudovirus neutralization assays (*36*) against eight variants of SARS-CoV-2: the
182 ancestral SARS-CoV-2 strain (WT), Delta (B.1.617.2), Lambda (C.37), Omicron BA.1
183 (B.1.1.529), BA.2, BA.4/5, BA. 2.75.2, BQ.1.1, and EG.5. The results showed that all four
184 antibodies neutralized all tested variants, with IC_{50} values ranging from 0.022 to 7.557 μg/mL
185 **(Fig. 1d and e)**. However, compared with the WT, obvious reductions in neutralization
186 activity were observed for Delta ($L452R_{SARS2}$), Lambda ($L452Q_{SARS2}$+$F490S_{SARS2}$), BA.4/5
187 ($L452R_{SARS2}$), BQ.1.1 ($L452R_{SARS2}$), and EG.5 ($F490S_{SARS2}$) variants containing $L452_{SARS2}$,
188 $F490_{SARS2,}$ or both mutations. By contrast, germline-like R1-32 lost neutralization (IC_{50} >10
189 μg/mL) against Delta, Lambda, BA.4/5, BQ.1.1, and EG.5 pseudoviruses.
190
191 Consistent with pseudovirus neutralization assays, C092, C807, BD56-104, and BD56-597
192 demonstrated potent neutralization (most IC_{50} <10 μg/mL) against authentic SARS-CoV-2
193 variants, including Delta ($L452R_{SARS2}$), BA.5 ($L452R_{SARS2}$), BQ.1($L452R_{SARS2}$),
194 XBB.1($F490S_{SARS2}$), and EG.5 ($F490S_{SARS2}$), while R1-32 showed no detectable
195 neutralization (IC_{50} >100 μg/mL) against these variants **(Fig. 1f and g)**. However, all five
196 antibodies lost neutralizing activities against the recent circulating variant KP.3.
197 Complementing the neutralization data, C092, C807, BD56-104, and BD56-597 exhibited
198 strong, non-dissociating binding to the S-trimers of variants neutralized in the neutralization
199 assays **(Fig. S2)**. Binding affinity assays revealed moderately weakened binding with
200 Lambda ($L452Q_{SARS2}$+$F490S_{SARS2}$), BA.4/5 ($L452R_{SARS2}$), and BQ.1.1 ($L452R_{SARS2}$) S-
201 trimers relative to WT, consistent with the observed reduction in neutralization potency
202 against these variants. Altogether, our neutralization and binding data demonstrate that C092,
203 C807, BD56-104, and BD56-597 exhibit markedly enhanced breadth and mutation tolerance
204 compared to the germline-like R1-32, maintaining neutralization activity against SARS-CoV-
205 2 variants carrying $L452_{SARS2}$, $F490_{SARS2,}$ or even both escape mutations, with minimal to
206 modest reductions in potency.
207

Binding of R1-32-like antibodies disassembles S-trimer without blocking ACE2 binding

To elucidate how C092, C807, BD56-104, and BD56-597 tolerate mutations to cross-neutralize SARS-CoV-2 variants, we prepared cryo-electron microscopy (cryo-EM) samples using stoichiometric mixtures of Fab, ACE2, and BA.4/5 S-trimer (Fab:ACE2:S-protomer = 1:1:1). Cryo-EM structures of C092, C807, BD56-104, and BD56-597 Fabs bound to BA.4/5 S-trimer in complex with ACE2 were determined (**Fig. 2a and Figs. S5-9**).

For the C092 Fab:ACE2:S-trimer sample, each S-trimer was found to adopt either 2 or 3 RBD "up" conformations, allowing simultaneous binding of either 2 or 3 Fab and ACE2 molecules. All other structures showed S-trimers with all three RBDs in the "up" position, with each RBD concurrently engaging both ACE2 and Fab **(Figs. S5-8)**. Consistent with previous conclusions (*27*), these S-trimer structures confirm that R1-32-like public antibodies do not interfere with ACE2 binding, in agreement with results from the antibody-ACE2 competition assays **(Fig. S3)**. In addition to ligand bound S-trimer structures, we also observed isolated S1 domains bound to both Fab and ACE2, suggesting that a portion of S-trimers disassembles upon simultaneous antibody and ACE2 binding. **(Figs. S5-8)**. Based on these disassembled particles, Structures of C092, C807, BD56-104, and BD56-597 bound to ACE2 bound S1 domain were determined to high-resolutions (2.58 - 2.83 Å) **(Fig. 2b and Figs. S5-9)**. We previously concluded that R1-32 neutralizes SARS-CoV-2 by inducing disassembly of S-trimers, thereby rendering them incapable of mediating membrane fusion (*27*). Based on the imaging data, we infer that C092, C807, BD56-104, and BD56-597 similarly retain the ability to induce disassembly of S-trimers from variant viruses.

R1-32-like antibodies impair spike fusogenic conformational change

To further confirm the neutralization mechanism, we conducted ligand-induced conformational change assays. The results showed that, like the WT, BA.4/5 S-trimers can be triggered by ACE2-Fc or YB9-258 (*37*), an epitope class 1 antibody that can mimic ACE2 function, to undergo the fusogenic conformational change, generating the proteinase K-resistant S2 fusion core **(Fig. S4a and c)**. ACE2-Fc retains the ability to trigger the EG.5.1 S-trimer, whereas YB9-258 loses this ability, likely due to epitope mutations in EG.5.1 that disrupt YB9-258 binding **(Fig. S4e)**. In line with our previous findings, S-trimers (WT, BA.4/5, and EG.5.1) pre-incubated with R1-32 and the four antibodies (C092, C807, BD56-104, and BD56-597) were unable to undergo structural transition into a post-fusion conformation **(Fig. S4a, c, and e).**

Further, assay results also showed that WT, BA.4/5, and EG.5 S-trimers pre-incubated with the four R1-32-like antibodies (C092, C807, BD56-104, or BD56-597) were unable to undergo the fusogenic conformational change upon subsequent addition of ACE2. **(Fig. S4b,**

247 **d, and f)**. In contrast, although R1-32 efficiently impairs the fusogenic conformational
248 change of the WT S-trimer, it only partially inhibits this transition in the BA.4/5 and EG.5 S-
249 trimers **(Fig. S4b, d, and f)**, likely due to the presence of $L452_{SARS2}$ or $F490_{SARS2}$ mutations
250 in these variants. This reduced inhibition correlates with R1-32's diminished neutralization
251 activity against the corresponding variants.
252
253 Together with our cryo-EM data showing disassembled S-trimers, the results from ligand-
254 induced conformational change assays confirm that the four identified R1-32-like antibodies
255 retain the ability to inhibit ACE2-induced fusogenic conformational changes of S-trimers
256 from variant viruses, likely by destabilizing or disassembling S-trimers, as previously
257 proposed for R1-32 against the WT virus (*27*). The results are further consistent with
258 neutralization assays demonstrating superior resilience of C092, C807, BD56-104, and
259 BD56-597 against $L452_{SARS2}$- and $F490_{SARS2}$-bearing variants compared to R1-32.
260

261 C092, C807, BD56-104, and BD56-597 recognize the same convergent
262 epitope as R1-32

263 The newly determined C092, C807, BD56-104, and BD56-597 complex structures were
264 aligned to our previously reported R1-32 complex structure (PDB: 7YDI), using the RBD as
265 the reference **(Fig. 2c)**. Based on this alignment, the root mean square deviations (RMSDs) of
266 the Fab variable regions were calculated as follows: C092 (1.5 Å), C807 (1.8 Å), BD56-104
267 (1.7 Å), and BD56-597 (1.5 Å). The low RMSD values indicate that these antibodies adopt
268 binding modes and recognize epitopes nearly identical to those of R1-32 **(Fig. 2c, left panel)**.
269
270 Antibody interface analysis reveals that all four R1-32-like antibodies engage the RBD
271 through both their heavy and light chains, with a predominant contribution from the heavy
272 chains: C092 binds an epitope area of 1,350 $Å^2$ (HC: 903 $Å^2$, LC: 447 $Å^2$); C807 binds an
273 epitope area of 1,193 $Å^2$ (HC: 820 $Å^2$, LC: 373 $Å^2$); BD56-104 binds an epitope area of 1,148
274 $Å^2$ (HC: 765 $Å^2$, LC: 383 $Å^2$); and finally BD56-597 binds an epitope area of 1,290 $Å^2$ (HC:
275 937 $Å^2$, LC: 353 $Å^2$). For comparison, the germline-like R1-32 binds an epitope area of
276 1,214 $Å^2$ (HC: 813 $Å^2$, LC: 401 $Å^2$).
277
278 All four R1-32-like antibodies utilize their characteristic IGHV1-69 HCDR2, featuring
279 hydrophobic residues at positions 52_H, 54_H, and 55_H (subscripts denote heavy (H) or light (L)
280 chain), to engage the hydrophobic RBD residues $F490_{SARS2}$ and $L492_{SARS2}$ (**Fig. 3a-d, left**
281 **panels**). Notably, within the epitopes of R1-32-like antibodies in the BA.4/5 RBD, the
282 epitope substitution $L452R_{SARS2}$ is present, with the aliphatic portion of $R452_{SARS2}$ sidechain
283 contacted by the hydrophobic HCDR2 residue 55_H. HCDR3 residues 102_H, 103_H, 104_H, and
284 107_H form polar interactions with RBD residues $E465_{SARS2}$, $R466_{SARS2}$, and $I468_{SARS2}$ (**Fig.**
285 **3a-d, right panels**). Additionally, HCDR1 (**Fig. 3a-d, left panels**) and LCDR1 (**Fig. 3a-d,**

286 **middle panels**) contribute to RBD binding in all four antibodies. Notably, in C092, unlike
287 the other three antibodies, both the light chain framework region 3 (LFR3) and LCDR3
288 participate in RBD binding (**Fig. 3a, middle panel**). Also notably, in BD56-104 and BD56-
289 597, the heavy chain backbone region 3 (HFR3) participates in RBD binding (**Fig. 3c and d,**
290 **left panels**).
291
292 We previously found that somatic hypermutation (SHM)-introduced residues play a key role
293 in enhancing antigen binding and conferring mutation tolerance (*22, 37*). Compared with the
294 germline antibody R1-32 (**Fig. S9e**), all four antibodies harbor SHM-introduced residues in
295 HCDR1 and LCDR1 (**Fig. 3a-d**). In C092, SHM-introduced residues are also present in
296 LFR3 and LCDR3 (**Fig. 3a**). In BD56-104 and BD56-597, SHM-introduced residues are also
297 found in heavy chain framework region 3 (HFR3) (**Fig. 3c and d**). Many of these residues
298 form additional contacts with the RBD, likely contributing to enhanced antigen binding (see
299 below).
300

301 Mutations tolerant R1-32-like antibodies share a convergent SHM pattern
302 enhancing antigen binding

303 C092, C807, BD56-104, and BD56-597 likely resist epitope mutations by having undergone
304 affinity maturation through somatic hypermutation. To investigate the affinity maturation
305 pathway underlying their mutation tolerance, we curated ninety-eight R1-32-like antibodies
306 from sequences reported by Cao *et al.*(*28*) and analyzed the correlation between SHM
307 patterns and neutralization activity (IC_{50} values). We examined whether specific mutations
308 are enriched in the R1-32-like antibodies isolated from individuals with different exposure
309 histories **(Fig. S10)**, as well as antibodies escaped by or tolerant to BQ.1.1 ($L452R_{SARS2}$) and
310 XBB ($F490S_{SARS2}$) **(Fig. 4a)**. We found several SHMs are highly enriched in R1-32-like
311 antibodies that tolerant to BQ.1.1 and XBB, such as $A33P/S_H$, $S35T_H$, and $N59D_H$ on the
312 heavy chain and $S26N_L$, $G52A/V_L$, and $S54N/T_L$ on the light chain **(Fig. 4a)**. In addition,
313 these SHMs were enriched in R1-32-like antibodies isolated from patients with breakthrough
314 infections (**Fig. S10**). Several of these SHM-enriched sites are also directly involved in
315 epitope binding in C092, C807, BD56-104, and BD56-597 (**Fig. 3**).
316
317 In the C092:RBD complex, SHM introduced HCDR1 residues $N31_H$ and $H32_H$ form a
318 hydrogen bond and a salt bridge with RBD residues $T470_{SARS2}$ and $E471_{SARS2}$, respectively
319 (**Fig. 3a, left panel**). SHM introduced HCDR1 residue $F33_H$ contacts RBD residues
320 $I468_{SARS2}$ and $Y351_{SARS2}$, as well as HCDR2 residue $I52_H$, thereby reinforcing the
321 hydrophobic interactions involving $I52_H$, $I54_H$, and $L55_H$ of HCDR2 and RBD residues
322 $F490_{SARS2}$ and $L492_{SARS2}$ (**Fig. 3a, left and right panels**). Additionally, SHM-introduced
323 residues in the light chain further enhance antigen binding: $N26_L$ of LCDR1 and $D70_L$ of
324 LFR3 form hydrogen bonds and salt bridges with $R357_{SARS2}$, while $D99_L$ of LCDR3 forms

325 salt bridges with $R346_{SARS2}$ **(Fig. 3a, middle panel)**. To confirm the function of the SHM-
326 introduced residues, we reverted them to their germline sequences and evaluated antigen
327 binding by the revertants. Reverting C092 HCDR1 to germline reduced binding to L452R,
328 Kappa ($L452R_{SARS2}$), Delta ($L452R_{SARS2}$), Lambda ($L452Q_{SARS2}$+$F490S_{SARS2}$), and BA.4/5
329 ($L452R_{SARS2}$) RBDs by ~ 10-fold (**Fig. 4b and Fig. S11a**). Likewise, reverting the light chain
330 SHM-introduced residues ($N26S_L$, $D70G_L$, and $D99G_L$) to germline reduced binding to the
331 same set of RBDs by ~10-100-fold.
332
333 In the C807:RBD complex, SHM-introduced HCDR1 residue $I33_H$ contacts RBD residues
334 $I468_{SARS2}$ and $Y351_{SARS2}$, as well as $I52_H$ of HCDR2, via hydrophobic interactions **(Fig. 3b,**
335 **left and right panels)**. Therefore, $I33_H$ of C807, like $F33_H$ in C092, enhances the
336 hydrophobic interactions mediated by HCDR2. Reverting HCDR1 of C807 into the germline
337 sequence reduced binding of RBDs with 452_{SARS2} and 490_{SARS2} mutations **(Fig. 4c and Fig.**
338 **S11b)**.
339
340 In the BD56-104:RBD complex, SHM-introduced HFR3 residue $D59_H$ forms salt bridges
341 with the mutated RBD residue $R452_{SARS2}$, while SHM-introduced HFR3 residue $E62_H$ forms
342 salt bridges with $R346_{SARS2}$ **(Fig. 3c, left panel)**. Germline reversion of HFR3 residues
343 ($D59N_H$ and $E62Q_H$) reduced binding to RBDs carrying 452_{SARS2} and 490_{SARS2} mutations. In
344 particular, the combined BD56-104 HFR3 revertant ($D59N_H/E62Q_H$) showed an ~100-fold
345 reduction in binding to the BA.4/5 RBD harboring the $L452R_{SARS2}$ mutation **(Fig. 4d and**
346 **Fig. S11c)**.
347
348 In the BD56-597:RBD complex, similar to C092 and C807, SHM-introduced HCDR1 residue
349 $P33_H$ provides extra hydrophobic interactions to enhance antigen binding **(Fig. 3d, left and**
350 **right panels)**. Further, similar to BD56-104, SHM-introduced HFR3 residue $D59_H$ forms salt
351 bridges with the mutated RBD residue $R452_{SARS2}$ **(Fig. 3d, left panel)**. Notably, SHM-
352 introduced LCDR1 residue $D26_L$ interacts with $R357_{SARS2}$ via salt bridges **(Fig. 3d, middle**
353 **panel)**. Germline reversion of HCDR1, HFR3 ($D59N_H$), and LCDR1 ($D26S_L$) reduced
354 binding to the RBDs carrying 452_{SARS2} and 490_{SARS2} mutations. Notably, towards the Lambda
355 RBD, carrying both $L452Q_{SARS2}$+$F490S_{SARS2}$ mutations, a 10-fold reduction in binding was
356 observed **(Fig. 4e and Fig. S11d)**.
357

358 ## HCDR3 contribute to mutation tolerance by R1-32-like antibodies

359 In addition to the extra interactions mediated by SHM-introduced residues, HCDR3 also
360 contributes to enhanced antigen binding in C092, C807, and BD56-597. Antigen-binding
361 assays showed that replacing the HCDR3s of C092, C807, or BD56-597 with that of R1-32
362 (97_H-ARENGYSGYGAA**A**NFDL-113_H, with $A109_H$ underlined in bold) markedly reduced
363 binding to the tested RBDs, with C807 being the most affected (**Fig. 4b-e and Fig. S11**). In

364 contrast, HCDR3 substitution in BD56-104 had a comparatively minor impact on binding.
365 Structural data revealed that the HCDR3s of C092, C807, and BD56-597 all contain a shared
366 $Y109_H$, which forms hydrogen bonds and hydrophobic interactions with RBD residues
367 $Y351_{SARS2}$ and $I468_{SARS2}$ (**Fig. 3a, b, and d, right panels**). Substituting $Y109_H$ with the
368 alanine present in R1-32 also notably impaired antigen binding in these three antibodies.
369 Moreover, combining HCDR1 germline reversion with the HCDR3 $Y109A_H$ substitution in
370 C092, C807, and BD56-597 produced an additive reduction in binding (**Fig. 4b-e and Fig.**
371 **S11**), indicating that distinct antigen-contact regions act synergistically to achieve high-
372 affinity binding.
373

374 Artificial affinity maturation of R1-32 validates SHM-introduced residues
375 in enhancing mutation tolerance

376 Our structural and antigen-binding data confirmed seven residues enriched with mutations
377 and associated with enhanced antigen binding, $A33F_H$, $N59D_H$, $Q62E_H$, and $A109Y_H$ in the
378 heavy chain, and $S26D_L$, $G70D_L$, and $G99D_L$ in the light chain. We introduced these residues
379 into R1-32 to generate an antibody called termed "R1-32-AAM" (R1-32-artificial-affinity-
380 matured). Notably, these SHM-introduced residues not only mediate additional RBD
381 interactions in C092, C807, BD56-104, and BD56-597, but most of them are also enriched in
382 R1-32-like antibodies that retain tolerance to BQ.1.1 and XBB (**Fig. 4a**).
383

384 Binding assays showed that R1-32-AAM exhibits markedly enhanced antigen-binding
385 activity compared with R1-32. Relative to R1-32, R1-32-AAM bound to RBDs bearing L452
386 mutation, including $L452R_{SARS2}$, Kappa ($L452R_{SARS2}$), Delta ($L452R_{SARS2}$), Lambda
387 ($L452Q_{SARS2}$+$F490S_{SARS2}$), BA.4/5 ($L452R_{SARS2}$), BF.7 ($L452R_{SARS2}$), and BQ.1.1
388 ($L452R_{SARS2}$) with faster association, slower dissociation, and resulting in ~100-fold
389 enhanced affinity (**Fig. 4f**). It also displayed enhanced binding to RBDs carrying $F490S_{SARS2}$
390 or $F490W_{SARS2}$, and XBB variant ($F490S_{SARS2}$), with ~10-100-fold higher affinity than R1-
391 32. Consistent with these binding data, R1-32-AAM neutralized authentic Delta
392 ($L452R_{SARS2}$), BA.5 ($L452R_{SARS2}$), XBB.1 ($F490S_{SARS2}$), and EG.5 ($F490S_{SARS2}$) viruses
393 (**Figs. 1f and g and 4g and h**), confirming that SHM-introduced residues enriched among
394 R1-32-like antibodies confer tolerance to $L452_{SARS2}$ and $F490_{SARS2}$ substitutions. Together
395 with structural differences to R1-32 (**Fig. S9e**), these findings indicate that the breadth of
396 C092, C807, BD56-104, and BD56-597 is largely attributable to affinity-maturation-
397 introduced residues, particularly within and around the CDRs, which mediate additional
398 antigen interactions.
399

Affinity maturation broadens the activity of R1-32-like antibodies toward SARSr-CoV RBDs

We further explored potential cross-reactivities of C092, C807, BD56-104, and BD56-597 toward SARSr-CoV RBDs using antigen-binding assays **(Fig. 5a and Fig. S12)**, testing representative type-1 to type-3 RBDs as previously defined by the extent of deletions within the receptor-binding motif (RBM) (*38*). All four antibodies bound the "type-1" RBDs of Pangolin-GD-2019, Bat-RaTG13, Pangolin-GX-2017, Laos-20-52, Laos-20-236, and Bat-RsSHC014 with affinities ranging from 0.016 to 48 nM. Notably, C092, C807, and BD56-597 cross-reacted to WIV1 RBD, whereas BD56-104 did not. Only C807 and BD56-597 bound the SARS-CoV-1 RBD, albeit with much compromised affinities (K_D < 341 nM) **(Fig. 5a)**. Remarkably, all four antibodies also bound the "type-2" BtKY72 RBD, despite its RBM sequence differing notably from the "type-1" SARS-CoV-2 RBD. Moreover, they retained binding to the "type-3" RBDs of GX2013, HeB2013, and RmYN02, which contain substantial loop deletions within the RBM region **(Fig. 5a)**. Among them, C092 and C807 exhibited tighter binding affinities than BD56-104 and BD56-597, demonstrating broader cross-reactivity towards SARSr-CoV RBDs. In contrast, R1-32 showed much weaker binding to the RBDs of Bat-RaTG13, Pangolin-GX-2017, and Bat-RsSHC014 (4.76-297 nM) than C092, C807, BD56-104, BD56-597, and failed to bind the RBDs of Bat-WIV1, SARS-CoV-1, BtKY72, GX2013, HeB2013, and RmYN02 **(Fig. 5a)**, indicating that affinity maturation confers broader SARSr-CoVs binding to R1-32-like antibodies.

We have established that C092, C807, BD56-104, and BD56-597 can well tolerate and maintain almost uncompromised neutralization towards variants carrying 1 mutation at RBD residues 452_{SARS2} or 346_{SARS2}, including Delta ($L452R_{SARS2}$), BA.5 ($L452R_{SARS2}$), and BA.2.75.2 ($R346T_{SARS2}$). Neutralization was somewhat reduced towards variants with 2 mutations within the RBD epitope, including Lambda ($L452Q_{SARS2}$+$F490S_{SARS2}$), BQ.1.1 ($R346T_{SARS2}$+$L452R_{SARS2}$), XBB.1 ($R346T_{SARS2}$+$F490S_{SARS2}$), and EG.5 ($R346T_{SARS2}$+$F490S_{SARS2}$) **(Fig. 1c-g)**. We noted that all four R1-32-like antibodies exhibited markedly impaired binding to the SARS-CoV-1 RBD. Within the R1-32-like antibody epitope, SARS-CoV-1 and SARS-CoV-2 differ at $L452_{SARS2}$, $F490_{SARS2}$, $R346_{SARS2}$, $R357_{SARS2}$, and $T470_{SARS2}$. To assess the mutation tolerance of the four R1-32-like antibodies **(Fig. S13)**, we introduced $R346T_{SARS2}$, $R357T_{SARS2}$, and $T470N_{SARS2}$ mutations into the Lambda ($L452Q_{SARS2}$+$F490S_{SARS2}$) RBD, towards which C092, C807, BD56-104, and BD56-597 already exhibited 9.5-178-fold reduction in binding affinity (**Fig. 1c)**. Introduction each single mutation into the Lambda RBD further reduced binding affinity by 4.6-59-fold (**Fig. S13b)**. We previously found that antibody neutralization is more impacted by reduced antigen association than by accelerated antigen dissociation, as the latter can be compensated by avidity (*22*). Notably, these mutated RBDs impacted both antibody association and dissociation, with association rates (k_{on}) reduced by 2.6-12-fold (**Fig. S13c)**, thereby 3 epitope

439 mutations likely impact neutralization. For BD56-104, Lambda+R346T$_{SARS2}$+T470N$_{SARS2}$,
440 completely abolished binding. For C092, C807, and BD56-597, we found that only when all
441 three mutations (R346T$_{SARS2}$, R357T$_{SARS2}$, and T470N$_{SARS2}$) were introduced simultaneously
442 into the Lambda RBD did the antibodies completely lose binding **(Fig. S13b and c)**. These
443 data suggest that C092, C807, BD56-104, and BD56-597 can still maintain antigen binding,
444 withstanding 3-4 mutations in the epitope.
445
446 To further investigate cross-reactivity, the C092 Fab and D1H4 Fab (*22*) were incubated with
447 the GX2013 S-trimer. Cryo-EM imaging of the sample revealed S-trimer disassembly. A 3.45
448 Å resolution structure of the C092 Fab:D1H4 Fab:GX2013 S1 complex was determined from
449 disassembled S-trimer particles **(Fig. 5b and c and Fig. S14)**. The complex was aligned to
450 the C092 Fab:BA.4/5 RBD complex using the RBDs as references to compare the difference
451 of C092 binding to GX2013 and BA.4/5 RBDs. The result shows that C092 binds to the same
452 epitope area on both the GX2013 and BA.4/5 RBDs **(Fig. 5d)**. C092 binds an epitope area of
453 1,003 Å^2 on GX2013 RBD, with 675 Å^2 buried by HCDRs, and 328 Å^2 buried by LCDRs.
454 This binding interface is smaller than the C092:BA.4/5 RBD interface (1,350 Å^2), consistent
455 with weaker binding of C092 to GX2013 RBD than BA.4/5.
456
457 In the C092:GX2013 RBD complex, the HCDR2 loop contains hydrophobic residues I52$_H$,
458 I54$_H$, and L55$_H$ and interacts with residues Y438$_{GX}$ (L452$_{SARS2}$), Y463$_{GX}$ (F490$_{SARS2}$), and
459 L465$_{GX}$ (L492$_{SARS2}$) on GX2013 RBD via hydrophobic interaction. These hydrophobic
460 interactions are further strengthened by the SHM-introduced HCDR1 residue F33$_H$ via extra
461 hydrophobic contacts **(Fig. 5e, left panels)**. The HCDR3 contacts GX2013 RBD residues -
462 E451$_{GX}$ (E465$_{SARS2}$), R452$_{GX}$ (R466$_{SARS2}$), L454$_{GX}$ (I468$_{SARS2}$) and Y342$_{GX}$ (Y351$_{SARS2}$),
463 with Y102$_H$, S103$_H$, G104$_H$, S107$_H$, and Y109$_H$ via extensive hydrogen bonds **(Fig. 5e, right**
464 **panel)**. Further, SHM-introduced HCDR1 N31$_H$ and LCDR1 N26$_L$ form hydrogen bonds
465 with S456$_{GX}$ (T470$_{SARS2}$) and K348$_{GX}$ (R357$_{SARS2}$), respectively, to strengthen antigen
466 binding. **(Fig. 5e, left and middle panel)**. Therefore, we conclude that affinity maturation is
467 a key driver for broadening the reactivity of R1-32-like antibodies toward SARSr-CoV
468 RBDs, with SHM-introduced residues mediating additional antibody-antigen interactions.
469

470 AI-based discovery of a ultrapotent and broadly R1-32-like neutralizing
471 antibody ZL525

472 Structure-guided artificial affinity maturation of R1-32 markedly enhanced its tolerance to
473 viral escape mutations, whereas natural affinity maturation broadened the activity of this
474 antibody class against sarbecoviruses with considerably diverged RBD epitopes, highlighting
475 their potential for further expansion of breadth against emerging SARS-CoV-2 variants.
476 Although C092, C807, BD56-104, and BD56-597 retained neutralizing activity against
477 variants generally with 2 epitope mutations, including Lambda (L452Q$_{SARS2}$+F490S$_{SARS2}$),

478 BQ.1.1 (R346T$_{SARS2}$+L452R$_{SARS2}$), XBB.1 (R346T$_{SARS2}$+F490S$_{SARS2}$), and EG.5
479 (R346T$_{SARS2}$+F490S$_{SARS2}$), the emerging KP.3 variant completely escaped their
480 neutralization (**Fig. 1f and g**).
481
482 To discover antibodies with broader reactivity, we employed an AI-driven approach to
483 discover R1-32-like antibodies with ultrapotent activities. We developed a deep learning
484 model to predict antibody-antigen binding affinity, followed by subsequent stratified virtual
485 screening to prioritize candidates (**Fig. 6a**). We pre-trained separate RoFormer-based (*39*)
486 language models for antibody heavy and light chains and antigen, using a masked amino acid
487 prediction task. Antigen representations were generated using the evolutionary-scale model
488 ESM2 (*40*). Embeddings from both antibody and antigen models were integrated through a
489 multilayer perceptron, followed by fine-tuning based on a consolidated antigen binding
490 affinity dataset.
491
492 The constructed affinity prediction model was used to screen 190 curated R1-32-like mAbs.
493 A lead candidate, ZL525, which derived from an individual with sequential BA.5 and XBB
494 breakthrough infections and exhibited higher predicted affinity than C092, C807, BD56-104,
495 and BD56-597 (**Fig. 6b**). Authentic virus neutralization assays showed that ZL525 effectively
496 neutralized all tested SARS-CoV-2 variants, including Beta, Delta, BA.1, BA.5, BQ.1,
497 XBB.1, EG.5, and KP.3, with IC_{50} values ranging from 0.044 to 7.193 μg/mL **(Fig. 6c and**
498 **d)**. Of note, ZL525 exhibited an excellent IC_{50} value of 0.107 μg/mL against KP.3, in
499 contrast to C092, C807, BD56-104, and BD56-597, which completely lost neutralizing
500 activity against the emerging KP.3 variant (IC_{50} > 100 μg/mL) **(Fig. 1f and g)**, underscoring
501 ZL525 as an ultrapotent broadly neutralizing antibody. Consistent with the neutralization
502 assays, ZL525 exhibited high affinities (below 0.71 nM) for the RBDs carrying L452$_{SARS2}$,
503 F490$_{SARS2}$, or both mutations, including Delta, Kappa, Lambda, BA.4/5, BQ.1.1, XBB.1.5,
504 and EG.5.1**(Fig. 6e and Fig. S16c)**. Furthermore, ZL525 maintained strong binding affinities
505 (below 1.11 nM) for newly emergent variants, including HK.3, JD.1.1, BA.2.86, JN.1, KP.2,
506 and KP.3, confirming its potential as a broad-spectrum therapeutic candidate. In addition,
507 ZL525 demonstrated enhanced cross-reactivity towards sarbecoviruses, by comparison with
508 C092, C807, BD56-104, and BD56-597, binding to all tested sarbecovirus RBDs, including
509 SARS-CoV-1(**Fig. 5a**).
510
511 To understand ZL525 mutation tolerance, the LP.8.1 S-trimer was incubated with ZL525 Fab
512 and ZL58 Fab (of a IGHV3-53 antibody). S-trimers in a 3-RBD "up" conformation with each
513 RBD bound to a ZL525 Fab and a ZL58 Fab were imaged. By focused refinement, a 2.93Å
514 ZL525 Fab: ZL58 Fab:LP.8.1 RBD complex structure was determined. **(Fig. 6f and Fig.**
515 **S15)**. As expected, ZL525 recognizes the convergent epitope bound by other R1-32-like
516 antibodies. Of note, its HCDR2 contains two characteristic SHM-introduced residues A55$_H$
517 and M57$_H$ to contact the RBD hydrophobic patch W452$_{SARS2}$, F490$_{SARS2}$, and L492 $_{SARS2}$ on

518 RBD **(Fig. 6f, left panel)**. Structural superposition of the BA.4/5 RBD:C092 and LP.8.1
519 RBD:ZL525 complexes reveals a conformational perturbation in the HCDR2 loop of ZL525.
520 This conformational perturbation appears to allow HCDR2 to better contact the mutated
521 L452W$_{SARS2}$ residue **(Fig. S16a).** The above hydrophobic interactions are further enhanced
522 by SHM-introduced HCDR1 residue P33$_H$. Similar to C092, SHM-introduced residues
523 LCDR1 residue N26$_L$ and LFR3 residue D70$_L$ form hydrogen bonds and salt bridges with
524 R357, respectively, to further enhance interaction **(Fig. 6f, middle panel)**. Compared with
525 C092, C807, BD56-104, and BD56-597, ZL525 exhibits a distinctive structural feature: SHM
526 introduced residues within HCDR2 (A55$_H$ and M57$_H$) directly contact epitope. Although
527 BD56-104 and BD56-597 contain SHM-introduced residues in HCDR2 (I51V$_H$ and A58P$_H$ in
528 BD56-104, A58T$_H$ in BD56-597), these residues are not involved in epitope contact with
529 their side-chains orienting away from the epitope.
530
531 Notably, our structure shows that the newly introduced N354$_{SARS2}$ glycosylation (*41, 42*)
532 maps directly onto the R1-32-like antibody epitope **(Fig. 6f, middle panel and Fig. S16b)**.
533 To test whether this glycan is involved in the shielding of R1-32 class of public antibodies,
534 we engineered T356K$_{SARS2}$ mutants of BA.2.86, JN.1, KP.2, and KP.3 RBDs to eliminate the
535 N354$_{SARS2}$ glycosylation. Remarkably, all four antibodies exhibited restored high-affinity
536 binding to these glycan-revertants, with markedly improved association rates (k_{on}) **(Fig.
537 S16d)**. Therefore, we confirm that the N354$_{SARS2}$ glycosylation contributes to the escape of
538 C092, C807, BD56-104, and BD56-597, consistent with its proposed role as an antigenic
539 change important for immune evasion in KP.3 (*43*).
540

541 ## Discussion

542 Through a series of structural and biochemical analyses, we now understand that affinity-
543 matured R1-32-like public antibodies, including C092 and C807 (*27*) as well as BD56-104
544 and BD56-597 (*28*), retain binding to their convergent epitope, tolerating the L452$_{SARS2}$ and
545 F490$_{SARS2}$ mutations through additional interactions mediated by SHM-introduced residues.
546 We further find that affinity-matured C092, C807, BD56-104, and BD56-597 maintain
547 neutralizing activity against viruses carrying at least two epitope mutations, exemplified by
548 the Lambda variant (L452Q$_{SARS2}$ + F490S$_{SARS2}$). Together, these findings show that affinity
549 maturation raises the genetic barrier to viral escape, such that the virus must acquire multiple
550 coordinated epitope substitutions to overcome neutralization. As a result, affinity-matured
551 antibodies may sustain protective immunity over longer periods, underscoring their essential
552 role in maintaining durable immune protection.
553
554 In addition, C092, C807, BD56-104, and BD56-597 exhibit broad cross-reactivity with a
555 diverse panel of SARS-related coronavirus (SARSr-CoV) RBDs, including Pangolin-GD-
556 2019 (*44*), Bat-RaTG13, Pangolin-GX-2017 (*45*), Laos-20-52, Laos-20-236 (*46*), Bat-

557 RsSHC014, Bat-WIV1(*47*), SARS-CoV-1(*48, 49*), BtKY72, GX2013, HeB2013, and
558 RmYN02 (*38*). This substantial expansion in breadth indicates that affinity maturation not
559 only enhances tolerance to SARS-CoV-2 epitope mutations but also extends the reactivity of
560 R1-32-like antibodies to antigenically diverse sarbecoviruses. The likely presence of such
561 affinity-matured public antibodies further suggests that a degree of pre-existing immunity to
562 diverse sarbecoviruses may now be present in the human population after the SARS-CoV-2
563 pandemic. The finding that affinity maturation broadens antibody reactivity toward
564 heterologous sarbecoviruses, with substantially diverged epitopes, provides a conceptual
565 framework for new strategies to design and discover broadly neutralizing antibodies that do
566 not necessarily rely on targeting highly conserved epitopes.
567
568 Furthermore, structural characterization of affinity matured R1-32-like public antibodies
569 revealed specific mutations relative to germline R1-32-like antibodies in and around the CDR
570 loops, including A33F_H, N59D_H, Q62E_H, A109Y_H, S26D_L, G70D_L, and G99D_L, that enhance
571 antigen binding, increase resilience to epitope mutations, and expand antibody breadth.
572 Notably, many of these sites (33_H, 59_H, 62_H, and 26_L) coincide with SHM-enriched sites in
573 R1-32-like antibodies that tolerate BQ.1.1 (L452R_{SARS2}) and XBB (F490S_{SARS2}), suggesting
574 convergent affinity-maturation patterns that promote increased resilience to antigenic drift.
575 We confirmed this concept by introducing mutations at these seven sites into R1-32 to
576 generate an artificially affinity-matured variant, R1-32-AAM, which exhibits improved
577 tolerance to the $L452_{SARS2}$ and $F490_{SARS2}$ mutations. These findings demonstrate how
578 deciphering in vivo maturation patterns can guide in vitro maturation strategies to enhance
579 antibody potency for therapeutic applications, as previously envisioned (*50*).
580
581 R1-32-like public antibodies utilize their characteristic IGHV1-69 germline-encoded
582 hydrophobic HCDR2 loops to bind a convergent epitope on the SARS-CoV-2 RBD, defined
583 by a hydrophobic patch formed by residues $L452_{SARS2}$, $F490_{SARS2}$, and $L492_{SARS2}$ (*16, 27*).
584 Likely owing to selection pressure from R1-32-like and other IGHV1-69 antibodies, residues
585 $L452_{SARS2}$ and $F490_{SARS2}$ have become antigenic mutation hotspots (*16, 51, 52*), impairing
586 antigen binding for most early-isolated R1-32-like antibodies that retained germline-like
587 sequences and lacked extensive affinity maturation (*16, 27*). The identification of R1-32-like
588 antibodies that are tolerant to epitope mutations implies that members of this class likely
589 remain active in the population and continue to exert immune pressure on this site. The
590 emergence of the novel $N354_{SARS2}$ glycosylation may reflect a viral adaptation to this
591 pressure, highlighting viral evolution potentially driven by this class of public antibodies.
592
593 Since the emergence of the BA.2.86 variant (**Fig. S16b**), the $N354_{SARS2}$ glycosylation
594 mutation has become fixed in circulating strains (*41, 43*). We have shown that the synergistic
595 effect of sequence variation and glycan-mediated structural occlusion enables viral escape
596 from previously identified mutation-tolerant R1-32-like antibodies (C092, C807, BD56-104,

597 and BD56-597). To identify antibodies with even stronger mutation-tolerance, we applied AI-
598 driven antibody language modelling and discovered an ultrapotent antibody, ZL525, which
599 retains strong neutralizing activity against the KP.3 variant carrying the $N354_{SARS2}$
600 glycosylation. Structural analysis indicates that SHM-introduced smaller or more flexible
601 hydrophobic residues ($L/F55A_H$ and $I/T57M_H$) in HCDR2 likely confer enhanced
602 conformational adaptability, allowing ZL525 to engage the altered hydrophobic surface
603 formed by $F490_{SARS2}$, $L492_{SARS2}$, and more importantly the substituted $L452W_{SARS2}$ (**Fig. 6f**),
604 while counteracting the shielding effect of the newly introduced $N354_{SARS2}$ glycan.
605 Moreover, ZL525 extends cross-reactivity to the SARS-CoV-1 S-protein, which is
606 substantially diverged from SARS-CoV-2. Together, these findings indicate that affinity
607 maturation can further evolve R1-32-like antibodies to acquire breadth that not only counters
608 viral escape but also enables cross-reactivity to more divergent sarbecoviruses.
609
610 The successful discovery of the ultrapotent broadly-neutralizing antibody ZL525 through AI-
611 driven language modelling highlights the transformative potential of machine learning in
612 accelerating antibody discovery. By decoding the functional patterns of somatic
613 hypermutations (SHMs) that confer broad neutralization, our study demonstrates how AI can
614 systematically infer critical sequence-structure-function relationships that might otherwise
615 require extensive experimental screening (*53*). This approach is particularly powerful for
616 targeting rapidly evolving pathogens, like SARS-CoV-2, where conventional antibody
617 discovery methods struggle to keep pace with viral escape variants (*54*). Recent advances in
618 deep learning-based protein modelling, such as AlphaFold and antibody-specific language
619 models, have begun to bridge the gap between sequence analysis and functional prediction
620 (*54*). Future integration of structural constraints with generative AI could further enhance the
621 precision of antibody optimization (*55*), paving the way for rapid discovery of antibody
622 therapeutics to counter emerging viral threats.
623
624 Finally, understanding the interplay between SARS-CoV-2 variant immune evasion and
625 antibody affinity maturation is essential for the development of more effective vaccination
626 and therapeutic strategies. Affinity-matured SARS-CoV-2 RBD-targeting antibodies that
627 have undergone extensive somatic hypermutation often exhibit enhanced neutralizing
628 potency, broader breadth, and increased resistance to viral mutations, suggesting that vaccine
629 regimens designed to promote stronger antibody affinity maturation may be desirable to
630 achieve more durable immune protection.

631 **Methods**

632 **COVID-19 patient and vaccine recipient enrollment**

633 Between December 2022 and December 2023, we enrolled a cohort of 64 individuals with
634 RT-PCR-confirmed SARS-CoV-2 infection. All participants had received three doses of an
635 inactivated COVID-19 vaccine (Sinopharm or CoronaVac) before experiencing sequential
636 breakthrough infections with the BA.5 and XBB subvariants, which corresponded to the two
637 major epidemic waves during this period. All participants provided written informed consent
638 before enrollment. The study was conducted under the approval and supervision of the Ethics
639 Committee of the First Affiliated Hospital of Guangzhou Medical University (Ethics IDs: ES-
640 2020-65).

641 **Cells and viruses**

642 Expi293F cells (Thermo Fisher Scientific, Cat# A14527) were cultured in FreeStyle^{TM}293
643 Expression Medium (Thermo Fisher Scientific, Cat# A1435101) in a shaking incubator at
644 37 °C with 8% CO_2. Human embryonic kidney (HEK) 293T (ATCC, Cat# CRL-3216),
645 HEK293T-ACE2, and Vero E6 cells (ATCC, Cat# CRL-1586) were cultured in 10% FBS-
646 supplemented Dulbecco's Modified Eagle's Medium (DMEM) at 37°C, 5% CO_2. Expi293F
647 cells were used for recombinant protein expression. HEK293T cells were used to generate
648 VSV-based pseudoviruses, while HEK293T-ACE2 and Vero E6 cells were used for
649 neutralization assays. VSV-based pseudotyped viruses were generated as previously
650 described (*36*). Authentic SARS-CoV-2 viruses, including WT, Beta, Delta, and Omicron
651 (BA.1, BA.4/5, BQ.1, XBB.1, EG.5, and KP.3), were isolated from clinical specimens of
652 COVID-19 patients and stored at the Guangzhou Customs District Technology Center BSL-3
653 laboratory. The SARS-CoV-2 Delta strain was kindly provided by the Guangdong Provincial
654 Center for Disease Control and Prevention, China. All experiments involving authentic
655 SARS-CoV-2 were conducted under biosafety level 3 (BSL-3) conditions at the Guangzhou
656 Customs District Technology Center BSL-3 Laboratory.
657

658 **Expression and purification of human monoclonal antibodies**

659 The heavy chain (IgH) and light chain (IgL) genes of antibodies were amplified and cloned
660 into the expression vector pCMV3 using ClonExpress Ultra One Step Cloning Kit (Vazyme,
661 C115). When the density of Expi293F cells reached 2.5×10^6 cells/mL, the paired IgH and
662 IgL plasmids were transiently co-transfected into the cells at a ratio of 1:1 using transfection
663 reagent Polyethylenimine (PEI). The transfected cells were transferred to a shaking incubator
664 at 33 °C with 8% CO_2. Five days post-transfection, the IgG was purified from the cell
665 supernatant using protein A affinity chromatography. Firstly, the supernatant was harvested
666 by centrifugation and incubated with Protein A Resin (Genscript, China) for 2 h to enable
667 antibody binding. After the resin was washed with PBS (Gibco), pH 7.4, the IgG bound to the

668 resin was eluted using 0.1 M citric acid, pH 3.0, and neutralized immediately with an equal
669 volume of 1 M Tris-HCl, pH 8.0, to maintain the pH within the neutral range. Subsequently,
670 the fractions containing IgG were concentrated and buffer-exchanged into PBS (pH 7.4)
671 using a 50 kDa MWCO Amicon Ultra filtration device (Merck Millipore). Purified antibodies
672 were aliquoted, flash-frozen, and stored at -80 °C until needed.
673

674 **Fab fragment production**

675 To produce Fab gene fragment, the VH and the human IgG1 constant region CH1 were
676 amplified from the IgH gene. The plasmids of paired Fab-IgH and IgL were transiently co-
677 transfected into the Expi293F cells at a ratio of 1:1 using the transfection reagent
678 Polyethylenimine (PEI) when the cell density reached 2.5×10^6 cells/mL. Five days post-
679 transfection at 33 °C, the culture supernatant was collected by centrifugation and incubated
680 with LambdaFabSelect (Cytiva) resin for 2 h to enable Fab binding. After the resin was
681 washed with PBS, the Fab bound to the resin was eluted with 0.1 M glycine (pH 2.0) into
682 1/2th volume 1 M Tris-HCl, pH 8.0, to maintain the pH within the neutral range.
683 Subsequently, the target elutions were concentrated by a 30 kDa MWCO Amicon Ultra
684 filtration device (Merck Millipore). Finally, the Fab was further purified and buffer-
685 exchanged into PBS using a Superdex 200 increase 10/300 GL column (Cytiva). Purified Fab
686 was aliquoted, flash frozen, and stored at −80 °C until needed.
687

688 **Expression and purification of SARS-CoV-2 S trimer and RBD**

689 SARS-CoV-2 Omicron BA.4/5 S trimer ectodomain (14-1211) with HexaPro (*56*) mutations
690 (F817P, A892P, A899P, A942P, K986P, and V987P) and deletion of amino acids "PRRA"
691 (681-684) at the fusion site was constructed into the expression vector pCDNA3.1 with an N-
692 terminal μ-phosphatase signal peptide and a C-terminal TEV-cleavage site, a T4 foldon
693 trimerization motif, and a hexahistidine tag (*57, 58*). Various SARS-CoV-2 variants S trimer
694 ectodomain (S-R) with "PRRA" (681-684) deletion at the fusion site were also constructed
695 using the same method. The coding sequence of SARS-CoV-2 RBD (residues 332-527) with
696 an N-terminal μ-phosphatase signal peptide and a C-terminal hexahistidine tag was cloned
697 into the expression vector pCDNA3.1 (*57*). All expression plasmids of S-trimer and RBD
698 were transiently transfected into Expi293F cells using transfection reagent Polyethylenimine
699 (*59*). Five days post-transfection at 33 °C, the cultural supernatant was collected and
700 supplemented with 25 mM phosphate, pH 8.0, 300 mM NaCl, 5 mM imidazole, and 0.5 mM
701 PMSF recirculated onto a HiTrap TALON crude column (Cytiva). Subsequently, the column
702 was washed with buffer A (25 mM phosphate, pH 8.0, 300 mM NaCl, 5 mM imidazole), and
703 target protein was eluted with a 100 mL linear gradient to 100% buffer B (25 mM phosphate,
704 pH 8.0, 300 mM NaCl, 500 mM imidazole). Fractions containing the target protein were
705 concentrated with an MWCO Amicon Ultra filtration device (Merck Millipore) and buffer-

706 exchanged into PBS. Additionally, all RBDs were further purified and buffer-exchanged into
707 PBS using a Superdex 75 increase 10/300 GL column (Cytiva) to remove RBD dimers. All
708 SARS-CoV-2 spike and RBD variants were purified as described above. Purified S-trimers
709 and RBDs were aliquoted, flash frozen, and stored at -80 °C until needed.
710

711 **Binding kinetics and affinity assessment of antibodies by BLI**

712 Binding kinetics and affinities of mAbs against SARS-CoV-2 spikes or RBDs and SARSr-
713 CoVs RBDs were assessed by Biolayer Interferometry (BLI) on an Octet RED96 instrument
714 (FortéBio, USA). The assays were performed at 25 °C, and all proteins were diluted to PBST
715 buffer (PBS with 1mg/mL BSA and 0.02% v/v Tween-20). Biosensors were pre-equilibrated
716 in the PBST buffer for 10 min before the experiments. Initially, antibodies (11 μg/mL) were
717 immobilized onto Protein A biosensors to a level of ~1.5 nm. After a 60 s baseline step in
718 PBST buffer, biosensors loaded with mAb were exposed (300 s) to the spikes (from 200 nM
719 to 3.125 nM in 2-fold serial dilutions) or various RBDs (200 nM) to measure association.
720 Subsequently, the biosensors were dipped into PBST (600 s) to measure dissociation of
721 spikes or RBDs from the biosensor surface. A blank reference was set for each reaction. Data
722 was reference-subtracted and analyzed using the FortéBio data analysis software HT
723 v12.0.2.59 (FortéBio) by fitting to single or double phase association and dissociation
724 kinetics to determine k_{on}, k_{off} and K_D. Raw data and fit data were plotted in GraphPad Prism
725 8.0.
726

727 **Antibody competition assay by BLI**

728 The competitive assays between antibodies or between antibodies and ACE2 were measured
729 by Biolayer Interferometry (BLI) using an Octet RED96 instrument (FortéBio, USA). All
730 experimental steps were performed at 25 °C. All proteins were diluted to PBST buffer (PBS
731 with 1mg/mL BSA and 0.02% v/v Tween-20), and anti-His biosensors were pre-equilibrated
732 in PBST buffer for 10 min before being immobilized with purified SARS-CoV-2 RBD-His
733 protein (30 μg/mL). Biosensors loaded with RBD were saturated with the first ligand
734 (antibodies or ACE2 with a concentration of 200nM), and then binding of the second ligand
735 (antibodies or ACE2 with a concentration of 200nM) or buffer as control was measured for
736 300 s. Data was analyzed using the FortéBio data analysis software HT v12.0.2.59 (FortéBio)
737 and raw data was plotted in GraphPad Prism 8.0.
738

739 **Pseudovirus neutralization assay**

740 The neutralization potency of antibodies against SARS-CoV-2 wild-type and multiple
741 variants (including Delta, Lambda, and Omicron sublineages BA.1, BA.2, BA.4/5,
742 BA.2.75.2, BQ.1.1, and EG.5) was evaluated using a pseudovirus neutralization test
743 following established protocols (*36*). The antibody samples were diluted to an initial

concentration of 10 μg/mL and subjected to eight gradient dilutions (3× serial dilutions), while the pseudovirus was diluted to 1.3×10^4 $TCID_{50}$/mL. After incubating the antibody samples and pseudovirus at 37 °C for 1 hour, HEK293T-ACE2 cells were added. After 24 hours of culture, luciferase detection reagent was added and placed in the multifunctional micropore detector (PE Ensight) to read the luminous value. Results were analyzed, and IC_{50} values were calculated by GraphPad Prism 8.0.

Authentic virus neutralization assay

All experiments involving authentic SARS-CoV-2 virus were conducted under biosafety level 3 (BSL-3) containment at the Guangzhou Customs District Technology Center. Antibodies were initially diluted to 100 μg/mL and then subjected to 4-fold serial dilutions. Each diluted mAb sample was combined with an equal volume of virus suspension containing 200 focus-forming units (FFU) of specified SARS-CoV-2 strains (WT, Beta, Delta, and Omicron subvariants BA.1, BA.4/5, BQ.1, XBB.1, EG.5, and KP.3). Mixtures were added to Vero E6 cells in 96-well cell culture plates for 1 h at 37 °C. After removal of the mixtures, fresh overlay medium consisting of MEM supplemented with 1.2% carboxymethylcellulose was added to each well. Following 24 hours of incubation, the overlay was discarded, and the cells were fixed with 4% paraformaldehyde (Biosharp, China, Cat# BL539A) and permeabilized using 0.2% Triton X-100 (Sigma, USA, Cat# T8787). Cells were incubated with a human anti-SARS-CoV-2 nucleocapsid protein monoclonal antibody (obtained by laboratory screening) at 37 °C for 1 h. After three washes with 0.15% PBST, cells were incubated with an HRP-labeled goat anti-human secondary antibody (Jackson ImmunoResearch Laboratories, Cat# 609-035-213) at 37 °C for 1 h. Following additional washes, foci were developed using TrueBlue Peroxidase Substrate (KPL, Gaithersburg, MD, Cat# 50-78-02), and counted with an ELISPOT reader (Cellular Technology Ltd. Cleveland, OH). The foci reduction neutralization test titer ($FRNT_{50}$) was calculated by the SpearmanKarber method.

Cryo-EM sample preparation and data collection

The BA.4/5 S-R/6P S-trimer was mixed with the corresponding Fab and ACE2 at a 3(S-protomer):3(Fab):3(ACE2) molar ratio for 1 minute to form the C092, C807, BD56-104, and BD56-597 Fab complexes. Similarly, the GX2013 S-trimer was mixed with C092 and D1H4, and the LP.8.1 S-trimer was mixed with ZL525 and ZL58, each at a 3:3:3 molar ratio for 1 minute to assemble the C092 Fab:D1H4 Fab:GX2013 S-trimer and ZL525 Fab:ZL58 Fab:LP.8.1 S-R/6P complexes, respectively. All mixtures contained 0.1% octyl glucoside, except for the C092 Fab:D1H4 Fab:GX2013 complex, which contained 0.05% octyl glucoside. Samples were loaded onto freshly glow-discharged (15 mA, 30 s) holey carbon grids (Quantifoil, Cu R1.2/R1.3) at 4 °C and 100% humidity. The grids were blotted for 2.5 s

782 with a force of 4 and samples were frozen immediately in liquid ethane using a Vitrobot
783 (Thermo Fisher).
784
785 For the C092 Fab:ACE2:Omicron BA.4/5 S-R/6P and C092 Fab:D1H4 Fab:GX2013 S-trimer
786 complexes, cryo-EM data were collected using a 200 keV Talos Arctica electron microscope
787 (ThermoFisher Scientific) equipped with a K3 direct electron detector (Gatan). Movies were
788 recorded using the SerialEM version 3.8.7 software at a nominal magnification of 45,000×
789 with a calibrated pixel size of 0.88 Å and a defocus range from -0.8 to -2.5 µm. Samples were
790 exposed for 1.83 s with a dose rate of 25.4 e^-/pixel/s fractionated over 27 frames, giving a
791 total electron dose of 60 $e^-/Å^2$.
792
793 To achieve higher resolution, a separately prepared C092 Fab:ACE2:BA.4/5 S-R/6P complex
794 was additionally imaged in a Titan Krios electron microscope (Thermo Fisher Scientific)
795 operating at 300 keV equipped with a SelectrisX energy filter (slit width 10 eV) and a Falcon
796 4 direct electron detector. The C807, BD56-104, and BD56-597 complexes, as well as the
797 ZL525 Fab:ZL58 Fab:LP.8.1 S-R/6P complex, were also imaged in the Titan Krios electron
798 microscope under the same setup. Movie stacks were automatically recorded using EPU with
799 the electron event representation (EER) mode at a nominal magnification of ×165,000 with a
800 calibrated pixel size of 0.73 Å and nominal defocus values ranging between -0.6 to -2.0 µm.
801 Each stack was recorded and exposed at a dose rate of 6.53 e−/pixel/s for 4.08 s resulting a
802 total dose of ~ 50 $e^-/Å^2$. All movie stacks were imported into cryoSPARC live
803 (v3.3.2/v4.2.0) (*60*) for pre-processing, which includes patched motion correction, contrast
804 transfer function (CTF) estimation, and bad image rejection.
805

806 ## Cryo-EM data processing

807 Data processing was carried out using cryoSPARC v3.3.2/v4.2.0. After removing bad
808 images, particles were picked by blob-picking on images and extracted for 2D Classification.
809 Well-defined 2D classes were selected as templates for template-picking.
810
811 For the C092 Fab:ACE2:BA.4/5 S-R/6P dataset collected at 200 keV **(Fig. S5)**, template-
812 picked particles were extracted and subjected to two rounds of 2D classification to remove
813 low-quality particles. Particles of either disassembled spike (S1) or Fab bound S-trimers were
814 separated by 2D classification into two sub-datasets. For the S1 sub-dataset, Ab-initio
815 Reconstruction was performed to generate initial 3D models, before the selected models were
816 used as references in Heterogeneous Refinement. A well-defined structure was constructed
817 by Non-uniform Refinement. To improve local resolution, a soft mask was applied to the
818 ACE2:RBD:Fab interface for Local Refinement, yielding a final map at 3.84 Å resolution.
819 For the S-trimer sub-dataset, three rounds of Ab-initial Reconstruction were conducted to
820 remove bad particles. All resulting models from the final round were used as references in

821 Heterogeneous Refinement. Particles generating highly similar structures were combined and
822 subject to Non-uniform Refinement. This process yielded two distinct S-trimer
823 reconstructions, featuring either 2 or 3 RBD "up" conformations, allowing simultaneous
824 binding of either 2 or 3 Fab and ACE2 molecules.
825
826 To improve resolution, a separate C092 Fab:ACE2:BA.4/5 S-R/6P complex dataset was
827 collected on a Titan Krios operating at 300 keV **(Fig. S6)**. Template-picked particles were
828 similarly split into S1 and S-trimer subsets via 2D classification. For the S1 sub-dataset, Ab-
829 initio Reconstruction and Heterogeneous Refinement were performed to generate 3D
830 reconstructions. To improve reconstruction, Topaz Training and Picking was performed
831 before picked particles were subjected to 2D Classification, Ab-initio Reconstruction, and
832 Heterogeneous Refinement again. The final particles were subjected to Non-uniform
833 Refinement, followed by Local Refinement with a mask focused on the ACE2:RBD:Fab
834 interface regions to yield a final map at 2.58 Å resolution. For the S-trimer sub-dataset
835 collected at 300 keV, A good 3D reconstruction was not obtained due to the absence of side-
836 view projections in 2D classes, even after Topaz picking.
837
838 For the C807/BD56-104/BD56-597 Fab:ACE2:BA.4/5 S-R/6P datasets **(Figs. S6 and S7)**,
839 Template-picked particles were similarly divided into two sub-datasets. The S1 sub-datasets
840 were processed in a workflow identical to the C092 Fab:ACE2:BA.4/5 S-R/6P S1 sub-dataset
841 collected at 300 keV. The S-trimer sub-datasets were processed using similar workflows,
842 each yielding a structure showing a S-trimer simultaneously bound by three Fabs and three
843 ACE2s. For the C807 Fab bound S-trimer sub-dataset, Topaz training was performed to
844 further pick S-trimer particles. The Topaz picked particles were subjected to 2D
845 Classification, Ab-initio Reconstruction, Heterogeneous Refinement, and Non-uniform
846 Refinement to reconstruct a final map. For the BD56-104 Fab bound S-trimer sub-dataset,
847 Topaz training and picking was performed after Heterogeneous Refinement. For the BD56-
848 597 S-trimer sub-dataset, reconstruction was obtained without performing Topaz picking.
849
850 For the C092 Fab:D1H4 Fab:GX2013 dataset collected at 200 keV **(Fig. S14)**, Fab bound S1
851 particles from disassembled S-trimers were template-picked before subjecting to 2D
852 Classification, Ab-initio Reconstruction, and Homogeneous Refinement. Topaz training and
853 picking were performed to further pick particles. The final reconstruction was obtained using
854 Topaz picked particles using Non-uniform Refinement, with a resolution of 3.45 Å.
855
856 For the ZL525 Fab:ZL58 Fab:LP.8.1 S-R/6P dataset **(Fig. S15)**, only Fab bound S-trimers
857 were observed by auto-picking and subsequent 2D classification. S-trimer particles were
858 subject to Ab-initio Reconstruction, Homogeneous Refinement, and Non-uniform
859 Refinement, imposing C3 symmetry to generate a map with a resolution of 2.75 Å. To
860 improve the resolution of the RBD:Fab interfaces, 3D classification with a focused mask

861 (ZL525 Fab:ZL58 Fab:LP.8.1 RBD) was applied to remove low-quality particles, followed
862 by Local Refinement. Ultimately, the focused ZL525 Fab:ZL58 Fab:LP.8.1 RBD map was
863 refined to a resolution of 2.93 Å.
864
865 All resolutions were estimated at the 0.143 criterion from phase-randomization-corrected
866 Fourier shell correlation (FSC) curves calculated between two independently refined half-
867 maps, multiplied by soft-edged solvent masks, in either RELION v4.0 or cryoSPARC (*60*).
868 Additional data processing details are summarized in **Figs. S5-8** and **Table S9**.
869

870 **Cryo-EM model building and structure refinement**

871 A previously determined structure of R1-32 Fab:ACE2:SARS-CoV-2 RBD complex (PDB:
872 7YDI) was fitted into the Cryo-EM map in UCSF Chimera v1.15 (*61*) and used as the starting
873 model for model building of the four complexes (C092/C807/BD56-104/BD56-597
874 Fab:ACE2:Omicron BA.4/5 RBD. Manual model building was carried out in Coot (*62*) in
875 order to adjust Ramachandran, rotamers, bond geometry restraints, etc. Structure refinement
876 was performed automatically using real-space refinement in PHENIX (*63*). For
877 C092/C807/BD56-104/BD56-597 Fab:ACE2:Omicron BA.4/5 S-timer complexes, the
878 structures (PDB:7YE5/7YEG) were used as initial model. For C092 Fab:D1H4 Fab:GX2013
879 RBD and ZL525 Fab:ZL58 Fab LP.8.1 RBD complexes, the structures (PDB:8ZY6 and
880 8WXL) were used as initial model respectively. Model validation statistics were summarized
881 in **Table S9**.
882

883 **Ligand-induced conformational change assay**

884 SARS-CoV-2 S-R spike at 1 mg/mL (7.09 μM) was incubated with ACE2-Fc or antibodies at
885 a 1:1.1 molar ratio for 1 h at room temperature. The samples were subsequently treated with
886 50 μg/mL proteinase K for 30 min at 4 °C. Non-reducing SDS-PAGE loading buffer (5×) was
887 added to each sample immediately before boiling at 98 °C for 5 min to stop the reaction.
888 Samples were separated by SDS–PAGE and transferred onto a PVDF membrane. After
889 blocking with 5% (w/v) skimmed milk in TBST buffer, the membrane was incubated with a
890 rabbit anti-SARS-CoV-2 S2 polyclonal antibody (1:2,500 dilution, Sino Biological, 40590-
891 T62) and subsequently with a goat anti-rabbit IgG conjugated to horseradish peroxidase
892 (1:1,000 dilution, Beyotime, A0208). The S proteins on the membrane were detected by
893 chemical luminescence using Pierce ECL western blotting substrate (Thermo Fisher, 32106).
894 To further assess the effect of non-ACE2 competing antibodies on S-R spike conformation,
895 the S-R spike protein was pre-incubated with antibodies (1 h), followed by incubation with
896 ACE2-Fc (1 h). Samples were analyzed by western blotting as described above.
897

Pre-trained antibody language models, ESM2 model, and virtual screening

Similar to our previously described Ab2binder model (*31*), we pre-trained antibody-specific language models on 1.4 billion antibody sequences sourced from the OAS database. After removing duplicate sequences and those containing non-canonical amino acids, the curated dataset consisted of 1.2 billion heavy chain and 210 million light chain sequences. Using the RoFormer (*39*) architecture, separate models were pre-trained for heavy and light chains. A Unique Amino Acid (UAA) tokenizer was adopted to represent each residue as a discrete token. Self-supervised learning was performed via a Masked Amino Acid (MAA) objective, in which randomly obscured residues were predicted from contextual cues, enabling the model to infer structural and functional properties of antibody sequences. To represent antigen inputs, we utilized the evolutionary-scale language model ESM2 (150M parameters), pre-trained on UniRef50 (*64*), to capture deep phylogenetic and structural features from protein sequences. Antigen embeddings were derived from ESM2 to encode functional constraints across diverse protein families. For antibody–antigen binding affinity prediction, features from both antibody chains, extracted using our pre-trained antibody models, were combined with ESM2-derived antigen embeddings. These representations were integrated via a multi-layer perceptron (MLP) to estimate binding affinities. The model was fine-tuned on a consolidated affinity dataset assembled from multiple public sources (*1, 12, 28, 32, 33, 65-68*), enhancing its capacity to discern subtle interactions between antibodies and antigenic variants. Finally, we applied the optimized model to screen a library of 190 R1-32-like monoclonal antibodies in silico, of which 102 antibodies were derived from published data and 88 antibodies were isolated from convalescent individuals. Detailed information on isolating the latter set of antibodies will be described in a separate study (*69*). Candidates were ranked by predicted affinity, and top-scoring antibodies were prioritized for experimental validation.

924 **Reference**

925 1. Y. Cao *et al.*, Imprinted SARS-CoV-2 humoral immunity induces convergent Omicron
926 RBD evolution. *Nature* **614**, 521-529 (2023).
927 2. C. D. Murin, I. A. Wilson, A. B. Ward, Antibody responses to viral infections: a
928 structural perspective across three different enveloped viruses. *Nat Microbiol* **4**, 734-
929 747 (2019).
930 3. Y. Cao *et al.*, Potent Neutralizing Antibodies against SARS-CoV-2 Identified by High-
931 Throughput Single-Cell Sequencing of Convalescent Patients' B Cells. *Cell* **182**, 73-
932 84.e16 (2020).
933 4. Y. Liu *et al.*, The N501Y spike substitution enhances SARS-CoV-2 infection and
934 transmission. *Nature* **602**, 294-299 (2022).
935 5. D. Mannar *et al.*, Structural analysis of receptor binding domain mutations in SARS-
936 CoV-2 variants of concern that modulate ACE2 and antibody binding. *Cell Rep* **37**,
937 110156 (2021).
938 6. R. Wang *et al.*, Analysis of SARS-CoV-2 variant mutations reveals neutralization
939 escape mechanisms and the ability to use ACE2 receptors from additional species.
940 *Immunity* **54**, 1611-1621.e1615 (2021).
941 7. M. Yuan *et al.*, Structural and functional ramifications of antigenicdrift in recent
942 SARS-CoV-2 variants. *science*, (2021).
943 8. D. Mannar *et al.*, SARS-CoV-2 Omicron variant: Antibody evasion and cryo-EM
944 structure of spike protein-ACE2 complex. *Science* **375**, 760-764 (2022).
945 9. C. O. Barnes *et al.*, SARS-CoV-2 neutralizing antibody structures inform therapeutic
946 strategies. *Nature* **588**, 682-687 (2020).
947 10. A. Sokal *et al.*, Maturation and persistence of the anti-SARS-CoV-2 memory B cell
948 response. *Cell* **184**, 1201-1213.e1214 (2021).
949 11. M. Yuan *et al.*, Structural basis of a shared antibody response to SARS-CoV-2. *Science*
950 **369**, 1119-1123 (2020).
951 12. F. Muecksch *et al.*, Affinity maturation of SARS-CoV-2 neutralizing antibodies confers
952 potency, breadth, and resilience to viral escape mutations. *Immunity* **54**, 1853-1868
953 e1857 (2021).
954 13. E. C. Chen *et al.*, Convergent antibody responses to the SARS-CoV-2 spike protein in
955 convalescent and vaccinated individuals. *Cell Rep* **36**, 109604 (2021).
956 14. Q. Yan *et al.*, Antibodies utilizing VL6-57 light chains target a convergent cryptic
957 epitope on SARS-CoV-2 spike protein and potentially drive the genesis of Omicron
958 variants. *Nat Commun* **15**, 7585 (2024).
959 15. Y. Zhang *et al.*, Analysis of B Cell Receptor Repertoires Reveals Key Signatures of the
960 Systemic B Cell Response after SARS-CoV-2 Infection. *J Virol* **96**, e0160021 (2022).
961 16. Q. Yan *et al.*, Shared IGHV1-69-encoded neutralizing antibodies contribute to the
962 emergence of L452R substitution in SARS-CoV-2 variants. *Emerg Microbes Infect* **11**,
963 2749-2761 (2022).
964 17. A. Patel *et al.*, Molecular basis of SARS-CoV-2 Omicron variant evasion from shared
965 neutralizing antibody response. *Structure* **31**, 801-811.e805 (2023).
966 18. C. I. Kaku *et al.*, Evolution of antibody immunity following Omicron BA.1
967 breakthrough infection. *Nat Commun* **14**, 2751 (2023).

19. Q. Yan *et al.*, Germline IGHV3-53-encoded RBD-targeting neutralizing antibodies are commonly present in the antibody repertoires of COVID-19 patients. *Emerg Microbes Infect* **10**, 1097-1111 (2021).
20. Q. Zhang *et al.*, Potent and protective IGHV3-53/3-66 public antibodies and their shared escape mutant on the spike of SARS-CoV-2. *Nat Commun* **12**, 4210 (2021).
21. M. Rapp *et al.*, Modular basis for potent SARS-CoV-2 neutralization by a prevalent VH1-2-derived antibody class. *Cell Rep* **35**, 108950 (2021).
22. B. Liu *et al.*, An unconventional VH1-2 antibody tolerates escape mutations and shows an antigenic hotspot on SARS-CoV-2 spike. *Cell Rep* **43**, 114265 (2024).
23. J. Dong *et al.*, Genetic and structural basis for SARS-CoV-2 variant neutralization by a two-antibody cocktail. *Nat Microbiol* **6**, 1233-1244 (2021).
24. M. Yuan *et al.*, Molecular analysis of a public cross-neutralizing antibody response to SARS-CoV-2. *Cell Rep* **41**, 111650 (2022).
25. Y. Wang *et al.*, A large-scale systematic survey reveals recurring molecular features of public antibody responses to SARS-CoV-2. *Immunity* **55**, 1105-1117.e1104 (2022).
26. K. Westendorf *et al.*, LY-CoV1404 (bebtelovimab) potently neutralizes SARS-CoV-2 variants. *Cell Rep* **39**, 110812 (2022).
27. P. He *et al.*, SARS-CoV-2 Delta and Omicron variants evade population antibody response by mutations in a single spike epitope. *Nat Microbiol* **7**, 1635-1649 (2022).
28. Y. Cao *et al.*, BA.2.12.1, BA.4 and BA.5 escape antibodies elicited by Omicron infection. *Nature* **608**, 593-602 (2022).
29. Q. Wang *et al.*, Alarming antibody evasion properties of rising SARS-CoV-2 BQ and XBB subvariants. *Cell* **186**, 279-286.e278 (2023).
30. H. Tegally *et al.*, Emergence of SARS-CoV-2 Omicron lineages BA.4 and BA.5 in South Africa. *Nat Med* **28**, 1785-1790 (2022).
31. H. He *et al.*, De novo generation of SARS-CoV-2 antibody CDRH3 with a pre-trained generative large language model. *Nat Commun* **15**, 6867 (2024).
32. C. Gaebler *et al.*, Evolution of antibody immunity to SARS-CoV-2. *Nature* **591**, 639-644 (2021).
33. Z. Wang *et al.*, Naturally enhanced neutralizing breadth against SARS-CoV-2 one year after infection. *Nature* **595**, 426-431 (2021).
34. Z. Wang *et al.*, mRNA vaccine-elicited antibodies to SARS-CoV-2 and circulating variants. *Nature* **592**, 616-622 (2021).
35. L. Zhang *et al.*, A proof of concept for neutralizing antibody-guided vaccine design against SARS-CoV-2. *Natl Sci Rev* **8**, nwab053 (2021).
36. J. Nie *et al.*, Quantification of SARS-CoV-2 neutralizing antibody by a pseudotyped virus-based assay. *Nat Protoc* **15**, 3699-3715 (2020).
37. H. Yu *et al.*, Somatically hypermutated antibodies isolated from SARS-CoV-2 Delta infected patients cross-neutralize heterologous variants. *Nat Commun* **14**, 1058 (2023).
38. J. Wang *et al.*, SARS-related coronavirus S-protein structures reveal synergistic RBM interactions underpinning high-affinity human ACE2 binding. *Sci Adv* **11**, eadr8772 (2025).
39. J. Su *et al.*, RoFormer: Enhanced transformer with Rotary Position Embedding. *Neurocomputing* **568**, 127063 (2024).
40. Z. Lin *et al.*, Evolutionary-scale prediction of atomic-level protein structure with a language model. *Science* **379**, 1123-1130 (2023).

1015 41. L. Li *et al.*, Spike structures, receptor binding, and immune escape of recently
1016 circulating SARS-CoV-2 Omicron BA.2.86, JN.1, EG.5, EG.5.1, and HV.1 sub-variants.
1017 *Structure* **32**, 1055-1067.e1056 (2024).
1018 42. H. Yang *et al.*, Structural basis for the evolution and antibody evasion of SARS-CoV-2
1019 BA.2.86 and JN.1 subvariants. *Nat Commun* **15**, 7715 (2024).
1020 43. P. Liu *et al.*, Spike N354 glycosylation augments SARS-CoV-2 fitness for human
1021 adaptation through structural plasticity. *Natl Sci Rev* **11**, nwae206 (2024).
1022 44. A. G. Wrobel *et al.*, Structure and binding properties of Pangolin-CoV spike
1023 glycoprotein inform the evolution of SARS-CoV-2. *Nat Commun* **12**, 837 (2021).
1024 45. S. Zhang *et al.*, Bat and pangolin coronavirus spike glycoprotein structures provide
1025 insights into SARS-CoV-2 evolution. *Nat Commun* **12**, 1607 (2021).
1026 46. X. Ou *et al.*, Host susceptibility and structural and immunological insight of S proteins
1027 of two SARS-CoV-2 closely related bat coronaviruses. *Cell Discov* **9**, 78 (2023).
1028 47. S. Qiao, X. Wang, Structural determinants of spike infectivity in bat SARS-like
1029 coronaviruses RsSHC014 and WIV1. *J Virol* **98**, e0034224 (2024).
1030 48. X. Zhang *et al.*, Disulfide stabilization reveals conserved dynamic features between
1031 SARS-CoV-1 and SARS-CoV-2 spikes. *Life Sci Alliance* **6**, (2023).
1032 49. Y. Yuan *et al.*, Cryo-EM structures of MERS-CoV and SARS-CoV spike glycoproteins
1033 reveal the dynamic receptor binding domains. *Nat Commun* **8**, 15092 (2017).
1034 50. S. Vajda, K. A. Porter, D. Kozakov, Progress toward improved understanding of
1035 antibody maturation. *Curr Opin Struct Biol* **67**, 226-231 (2021).
1036 51. P. Pushparaj *et al.*, Immunoglobulin germline gene polymorphisms influence the
1037 function of SARS-CoV-2 neutralizing antibodies. *Immunity*, (2022).
1038 52. T. N. Starr, A. J. Greaney, A. S. Dingens, J. D. Bloom, Complete map of SARS-CoV-2
1039 RBD mutations that escape the monoclonal antibody LY-CoV555 and its cocktail with
1040 LY-CoV016. *Cell Rep Med* **2**, 100255 (2021).
1041 53. S. Shan *et al.*, Deep learning guided optimization of human antibody against SARS-
1042 CoV-2 variants with broad neutralization. *Proc Natl Acad Sci U S A* **119**, e2122954119
1043 (2022).
1044 54. T. A. Desautels *et al.*, Computationally restoring the potency of a clinical antibody
1045 against Omicron. *Nature* **629**, 878-885 (2024).
1046 55. V. R. Shanker, T. U. J. Bruun, B. L. Hie, P. S. Kim, Unsupervised evolution of protein
1047 and antibody complexes with a structure-informed language model. *Science* **385**, 46-
1048 53 (2024).
1049 56. C. L. Hsieh *et al.*, Structure-based design of prefusion-stabilized SARS-CoV-2 spikes.
1050 *Science* **369**, 1501-1505 (2020).
1051 57. X. Xiong *et al.*, A thermostable, closed SARS-CoV-2 spike protein trimer. *Nat Struct*
1052 *Mol Biol* **27**, 934-941 (2020).
1053 58. K. Qu *et al.*, Engineered disulfide reveals structural dynamics of locked SARS-CoV-2
1054 spike. *PLoS Pathog* **18**, e1010583 (2022).
1055 59. H. Yuan *et al.*, Structures and receptor binding activities of merbecovirus spike
1056 proteins reveal key signatures for human DPP4 adaptation. *Sci Adv* **11**, eadv7296
1057 (2025).
1058 60. A. Kucukelbir, F. J. Sigworth, H. D. Tagare, Quantifying the local resolution of cryo-EM
1059 density maps. *Nat Methods* **11**, 63-65 (2014).
1060 61. E. F. Pettersen *et al.*, UCSF Chimera--a visualization system for exploratory research
1061 and analysis. *J Comput Chem* **25**, 1605-1612 (2004).

1062 62. P. Emsley, B. Lohkamp, W. G. Scott, K. Cowtan, Features and development of Coot.
1063 *Acta Crystallogr D Biol Crystallogr* **66**, 486-501 (2010).
1064 63. P. V. Afonine *et al.*, Real-space refinement in PHENIX for cryo-EM and
1065 crystallography. *Acta Crystallogr D Struct Biol* **74**, 531-544 (2018).
1066 64. B. E. Suzek, Y. Wang, H. Huang, P. B. McGarvey, C. H. Wu, UniRef clusters: a
1067 comprehensive and scalable alternative for improving sequence similarity searches.
1068 *Bioinformatics* **31**, 926-932 (2015).
1069 65. Y. Cao *et al.*, Omicron escapes the majority of existing SARS-CoV-2 neutralizing
1070 antibodies. *Nature* **602**, 657-663 (2022).
1071 66. Z. Wang *et al.*, Memory B cell responses to Omicron subvariants after SARS-CoV-2
1072 mRNA breakthrough infection in humans. *J Exp Med* **219**, (2022).
1073 67. L. Witte *et al.*, Epistasis lowers the genetic barrier to SARS-CoV-2 neutralizing
1074 antibody escape. *Nat Commun* **14**, 302 (2023).
1075 68. C. I. Kaku *et al.*, Recall of preexisting cross-reactive B cell memory after Omicron BA.1
1076 breakthrough infection. *Sci Immunol* **7**, eabq3511 (2022).
1077 69. Q. Yan *et al.*, AI recognizes convergent somatic hypermutation signatures to allow
1078 the discovery of variant-resilient broadly neutralizing antibodies. *bioRxiv*,
1079 2025.2012.2010.693372 (2025).
1080

Data availability

Cryo-EM density maps for the structures of R1-32-like antibodies in complex with S-trimer or S1 fragment have been deposited in the Electron Microscopy Data Bank (EMDB) with accession codes EMD-66890, EMD-66891, EMD-66892, EMD-66893, EMD-66894, EMD-66895, EMD-66896, EMD-66897, EMD-66898, EMD-66899, EMD-66900, and EMD-66901. Related atomic models have been deposited in the Protein Data Bank (PDB) under accession codes 9XHY, 9XHZ, 9XI0, 9XI1, 9XI2, 9XI3, 9XI4, 9XI5, 9XI6, 9XI7, 9XI8, and 9XI9, respectively.

Acknowledgements

We thank the staff of the GIBH-CAS Cryo-EM Facility for their help with cryo-EM sample preparation and data collection. We thank the staff of the Guangzhou Laboratory Cryo-EM Facility for their help with cryo-EM sample data collection. This work was supported by the National Key R&D Program of China (2021YFA1300903 to X.X.); the National Natural Science Foundation of China (82341085 and 32570199 to X.X., 82495200 and 82495203 to J.Z., 32361163669, 32170189, and 32241021 to J.H., 92469301 to L.C., 82201932 to Q.Y.); the Emergency Key Program of Guangzhou Laboratory (EKPG21-06 to X.X.); Major Project of Guangzhou National Laboratory (SRPG22-002 to X.X., EKPG21-30-2 to J.Z.); the Guangdong Basic and Applied Basic Research Foundation (2021A1515011289 to X.X.); the Science and Technology Planning Project of Guangdong Province, China (2023B1212060050 and 2023B1212120009 to X.X.); the Basic Research Project of Guangzhou Institutes of Biomedicine and Health, Chinese Academy of Sciences (GIBHBRP24-02 to X.X.); the 111 Project (D18010 to J.Z.); the Natural Science Fund of Guangdong Province (2025A1515011245 to B.L.); the Young Doctoral Starting Sail Project of the Guangzhou Municipal Science and Technology Bureau (2024A04J4195 to B.L.). X.X. acknowledges Start-up grants from the Chinese Academy of Sciences.

Contributions

Q.Y., C.N., X.H., and B.L. conceived the study under the direction of X.X. and J.Z.; Q.Y. performed the initial antibody analysis and screening from the published data; C.N., B.L., X.H. and P.H. expressed and purified antibodies; B.L., C.N., and J.W. purified spikes and RBDs for cryo-EM and other experiments using constructs and protocols developed by X.X.; C.N., B.L., and L.W. performed BLI assays; X.H., H.Z., and Y.Y. performed pseudovirus and authentic virus neutralization assays; C.N. performed western blots to assay spike structural change; C.N., B.L., X.G., H.Y., and B.Z. preformed cryo-EM sample preparation and collected cryo-EM data under the supervision of J.H. and X.X.; X.G., C.N., and Z.L. processed cryo-EM data under the supervision of J.H. and X.X.; X.X., C.N., and B.L. analysed cryo-EM structures with assistance from X.G. and Q.Y.; Y.S., Q.Y., Y.Y., and F.W.

performed AI-based antibody discovery under the supervision of J.Y.; C.N., Q.Y., B.L., X.G. and X.H. prepared the figures under the supervision of X.X. and J.H.; X.X., C.N., and Q.Y. wrote the paper with input from all co-authors; G.H. and X.H. reviewed and edited the manuscript. X.X., Z.J., J.Y., J.H., L.C., and X.C. supervised the research.

Competing interests

The authors declare that they have no competing interests.

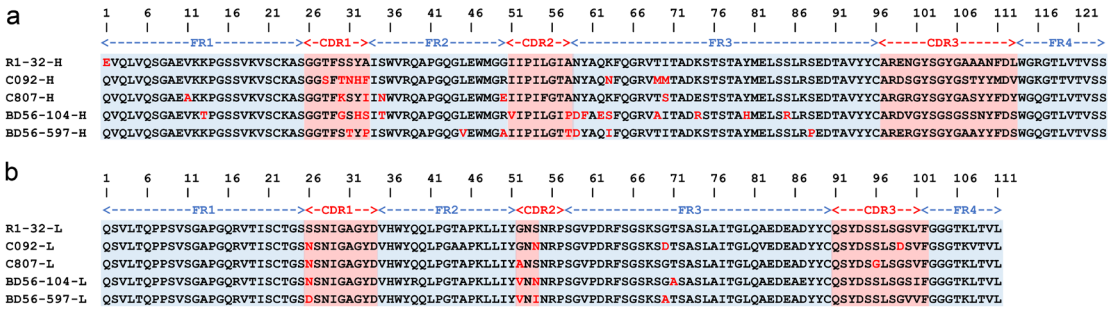

c

	WT	K417N	K417T	E484K	E484Q	T478K	L452R	L452Q	L452M	F490S	Alpha	Beta	Gamma	Kappa	Delta	Lambda
C092	0.046 (1.0)	0.093 (2.0)	0.019 (2.4)	0.042 (1.1)	0.048 (1.0)	0.058 (1.3)	0.072 (1.6)	0.200 (4.3)	0.040 (1.2)	0.128 (2.8)	0.050 (1.1)	0.093 (2.0)	0.096 (2.1)	0.127 (2.8)	0.179 (3.9)	0.436 (9.5)
C807	0.118 (1.0)	0.221 (1.9)	0.157 (1.3)	0.198 (1.7)	0.168 (1.4)	0.164 (1.4)	1.08 (9.2)	1.18 (10.0)	0.246 (2.1)	0.437 (3.7)	0.142 (1.2)	0.160 (1.4)	0.153 (1.3)	0.813 (6.9)	0.904 (7.7)	4.36 (36.9)
BD56-104	0.038 (1.0)	0.073 (1.9)	0.098 (2.6)	0.070 (1.8)	0.088 (2.3)	0.073 (1.9)	0.048 (1.3)	0.349 (9.2)	0.027 (1.4)	0.592 (15.6)	0.027 (1.4)	0.046 (1.2)	0.036 (1.1)	0.091 (2.4)	0.082 (2.2)	6.76 (178)
BD56-597	0.048 (1.0)	0.044 (1.1)	0.057 (1.2)	0.047 (1.0)	0.063 (1.3)	0.050 (1.0)	0.079 (1.6)	0.108 (2.3)	0.031 (1.5)	0.105 (2.2)	0.050 (1.0)	0.014 (3.4)	0.016 (3.0)	0.037 (1.3)	0.035 (1.4)	0.560 (11.7)
R1-32	0.931 (1.0)	1.13 (1.2)	N/A	3.55 (3.8)	2.96 (3.2)	2.12 (2.3)	54.2 (58.2)	34.9 (37.5)	N/A	11.8 (12.7)	0.709 (1.3)	10.3 (11.0)	N/A	92.1 (98.9)	72.6 (78.0)	953 (1023)

	BA.1	BA.1.1	BA.2	BA.3	BA.2.75	BA.2.75.2	BA.2.11	BA.2.12.1	BA.2.13	BA.4/5	BF.7	BQ.1.1	XBB	XBB.1.5	EG.5	EG.5.1
C092	0.142 (3.1)	0.016 (2.9)	0.022 (2.1)	0.032 (1.4)	0.017 (2.7)	0.085 (1.8)	0.032 (1.4)	0.213 (4.6)	0.022 (2.1)	0.132 (2.9)	0.293 (6.4)	0.200 (4.3)	0.056 (1.2)	0.073 (1.6)	0.056 (1.2)	0.059 (1.3)
C807	0.224 (1.9)	0.081 (1.5)	0.014 (8.4)	0.049 (2.4)	0.048 (2.5)	0.148 (1.3)	0.471 (4.0)	0.215 (1.8)	0.044 (2.7)	0.741 (6.3)	1.91(16.2)	2.01 (17.0)	0.194 (1.6)	0.640 (5.4)	0.653 (5.5)	0.677 (5.7)
BD56-104	0.122 (3.2)	0.024 (1.6)	0.021 (1.8)	0.031 (1.2)	0.099 (2.6)	0.167 (4.4)	0.049 (1.3)	0.087 (2.3)	0.020 (1.9)	0.029 (1.3)	0.598(15.7)	0.897 (23.6)	2.11 (55.5)	4.35 (114)	4.25 (112)	4.40 (116)
BD56-597	0.067 (1.4)	0.027 (1.8)	0.046 (1.0)	0.031 (1.5)	0.048 (1.0)	0.079 (1.6)	0.016 (3.0)	0.021 (2.3)	0.019 (2.5)	0.051 (1.1)	0.061 (1.3)	0.097 (2.0)	0.070 (1.5)	0.034 (1.4)	0.043 (1.1)	0.051 (1.1)
R1-32	1.13 (1.2)	N/A	N/A	N/A	N/A	N/A	N/A	N/A	N/A	55.5 (59.6)	129 (138)	212 (228)	49.2 (52.8)	N/A	N/A	N/A

Fold change relative to RBD-WT | affinity ≥ WT | Fold change < 10 | Fold change 10-100 | Fold change > 100

d

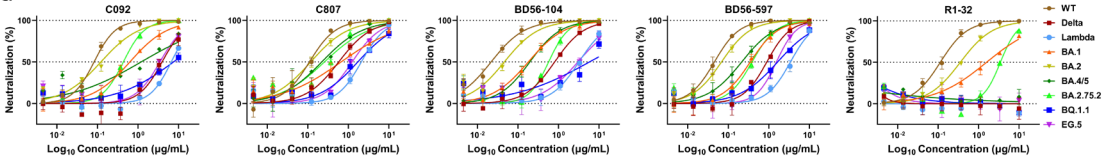

e

mAb	Pseudoviruses neutralization IC50 (μg/mL)								
	WT	Delta	Lambda	BA.1	BA.2	BA.4/5	BA.2.75.2	BQ.1.1	EG.5
C092	0.083	3.931	6.633	0.633	0.122	1.200	0.437	7.557	3.484
C807	0.110	0.582	2.095	0.665	0.118	0.222	0.259	1.717	1.245
BD56-104	0.022	0.807	3.211	0.181	0.046	0.197	0.574	5.844	3.026
BD56-597	0.046	0.896	3.427	0.350	0.068	0.216	0.387	1.654	1.542
R1-32	0.113	>10	>10	1.576	0.354	>10	3.465	>10	>10

f

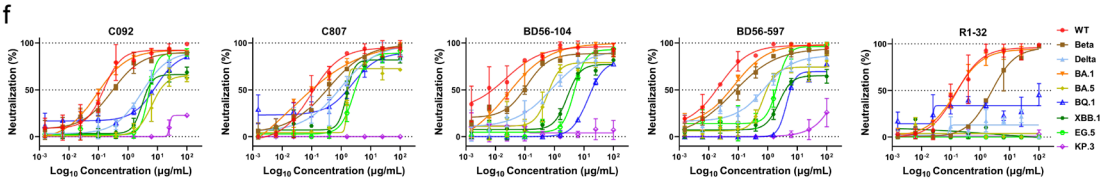

g

mAb	Authentic viruses neutralization IC50 (μg/mL)								
	WT	Beta	Delta	BA.1	BA.5	BQ.1	XBB.1	EG.5	KP.3
C092	0.151	0.293	2.878	0.085	6.329	8.575	3.042	5.004	>100
C807	0.094	0.356	0.944	0.021	1.578	2.401	1.517	2.671	>100
BD56-104	0.023	0.114	0.819	0.025	0.577	13.680	2.698	4.676	>100
BD56-597	0.023	0.067	0.765	0.073	0.693	4.310	2.376	2.099	>100
R1-32	0.151	2.343	>100	0.142	>100	>100	>100	>100	>100

Fig. 1. Sequence alignments, binding affinities, and neutralization activities of R1-32-like antibodies.

a-b, Heavy chain (**a**) and Light chain (**b**) sequence alignments of germline-like R1-32 with selected affinity-matured R1-32-like antibodies (C092, C807, BD56-104, BD56-597). The sequences of R1-32 are used as the references, with somatic hypermutation-derived amino

1131 acids marked in red. The HCDRs and LCDRs residues are highlighted in salmon. **c**, Binding
1132 affinities of R1-32-like antibodies to a panel of SARS-CoV-2 RBDs. Binding assays were
1133 performed using biolayer interferometry (BLI). Dissociation constant K_Ds (nM) are shown,
1134 with fold changes relative to wild-type RBD indicated in parentheses. RBDs carrying L452,
1135 F490, or both substitutions are colored in red, blue, and purple, respectively. Binding
1136 affinities higher than the wild-type RBD are shown in blue, whereas reduced affinities (<10-
1137 fold, 10-100-fold, and >100-fold relative to wild-type) are shown in green, yellow, and
1138 orange, respectively. For R1-32, the K_Ds of Alpha, Beta, BA.1, K417N, E484K/Q, T478K,
1139 and L452Q were obtained from our previously published work (*27*). N/A means untested.
1140 RBD binding curves are shown in **Fig. 4f and Fig. S1b-e,** and K_D data used for comparisons
1141 are shown in **Tables S1 and S4**. **d**, Neutralization activities of R1-32-like antibodies towards
1142 SARS-CoV-2 wild-type, Delta, Lambda, Omicron BA.1, BA.2, BA.4/5, BA.2.75.2, and
1143 BQ.1.1 pseudoviruses. Data are presented as mean ± SD (n = 2). IC_{50} values are summarized
1144 in **e**. **f**, Neutralization activities of R1-32-like antibodies towards WT, Beta, Delta, Omicron
1145 BA.1, BA.5, BQ.1, XBB.1, EG.5, and KP.3 authentic viruses. Data are presented as mean ±
1146 SD (n = 2). IC_{50} values are summarized in **g.**

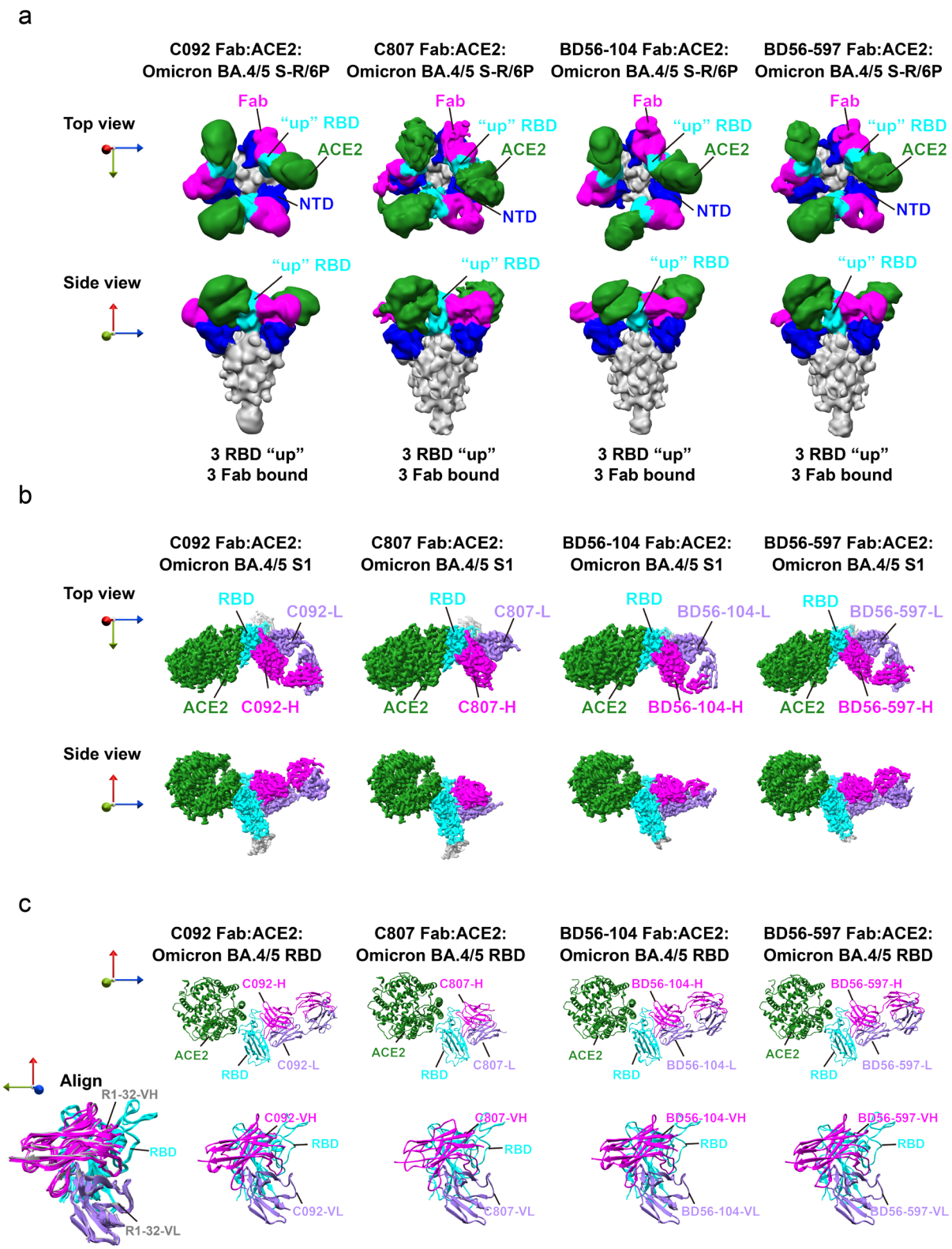

Fig. 2. Structures of C092, C807, BD56-104, and BD56-597 in complex with SARS-CoV-2 BA.4/5 S-trimer and ACE2.

a, Cryo-EM densities (low-pass filtered to 12 Å) of BA.4/5 S-R/6P S-trimer bound to Fab and ACE2 at 3:3:3 molar ratio. C092, C807, BD56-104, and BD56-597 Fabs, NTD, RBD, and ACE2 are colored in magenta, blue, cyan, and dark green, respectively; the rest of the S-

trimer is colored in grey. The 3 RBDs in “up” positions are indicated, each simultaneously engaging both ACE2 and antibody. **b**, Cryo-EM densities of BA.4/5 S1 bound to Fab and ACE2. C092, C807, BD56-104, and BD56-597 Fab-HC, Fab-LC, NTD, RBD, and ACE2 are colored in magenta, purple, blue, cyan, and dark green, respectively; the rest of the S1 is colored in grey. **c**, Structures of the BA.4/5 RBD:Fab:ACE2 complex (**upper panels**) derived from the density shown in panel **b**. Individual binding modes of C092, C807, BD56-104, and BD56-597 to the RBD are shown in the lower panels. Superposition of C092, C807, BD56-104, BD56-597, and R1-32 bound to RBD is shown in the left panels, with C092, C807, BD56-104, and BD56-597 Fabs rendered in color and the R1-32 Fab shown in grey.

a

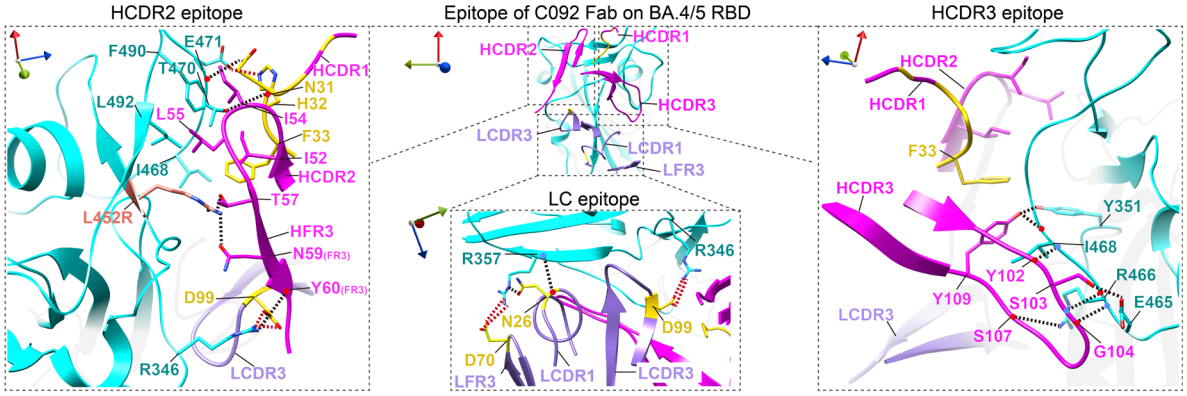
HCDR2 epitope
Epitope of C092 Fab on BA.4/5 RBD
HCDR3 epitope
F490
E471
T470
HCDR1
N31
H32
L492
L55
I54
F33
I52
I468
HCDR2
T57
L452R
HFR3
N59(FR3)
Y60(FR3)
D99
R346
LCDR3
HCDR2
HCDR1
HCDR3
LCDR3
LCDR1
LFR3
LC epitope
R357
R346
N26
D99
D70
LFR3
LCDR1
LCDR3
HCDR2
HCDR1
F33
HCDR3
Y351
I468
Y102
R466
Y109
S103
E465
LCDR3
S107
G104

b

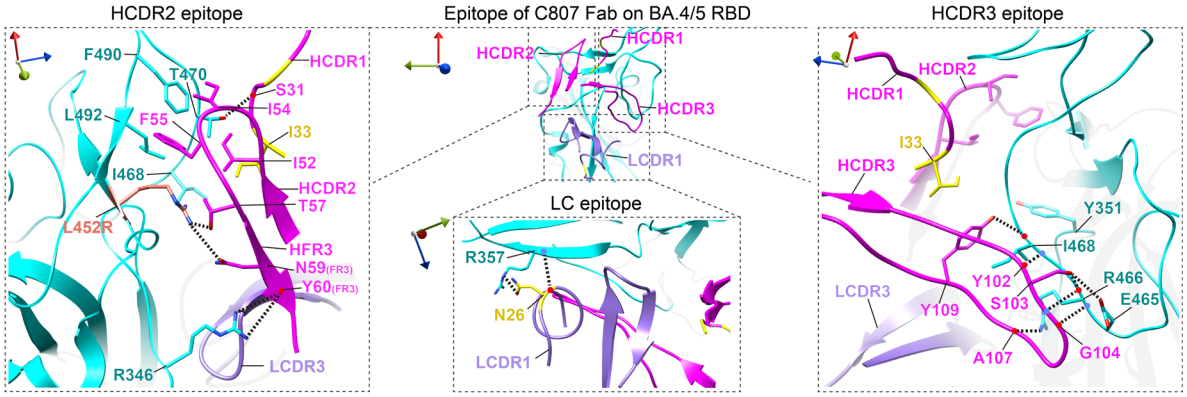
HCDR2 epitope
Epitope of C807 Fab on BA.4/5 RBD
HCDR3 epitope
F490
T470
HCDR1
S31
L492
F55
I54
I33
I52
I468
HCDR2
T57
L452R
HFR3
N59(FR3)
Y60(FR3)
R346
LCDR3
HCDR2
HCDR1
HCDR3
LCDR1
LC epitope
R357
N26
LCDR1
HCDR2
HCDR1
I33
HCDR3
Y351
I468
Y102
R466
LCDR3
Y109
S103
E465
A107
G104

c

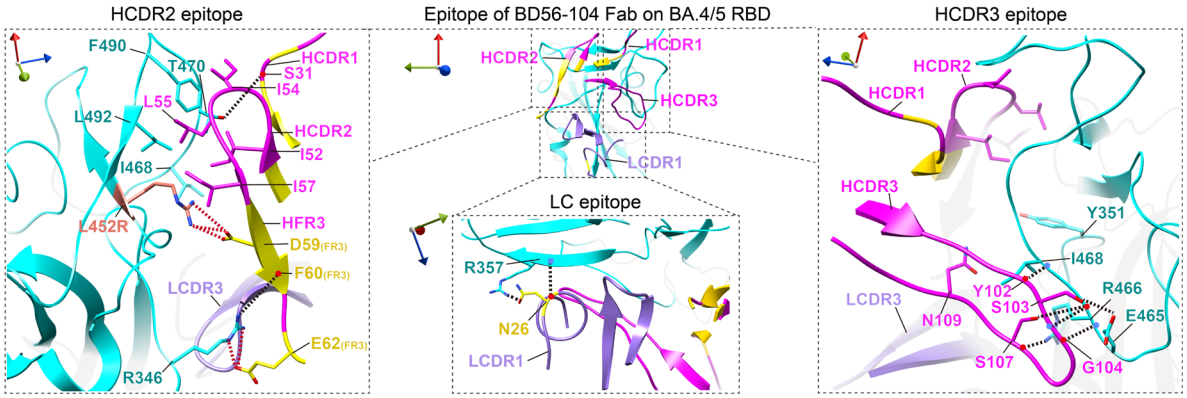
HCDR2 epitope
Epitope of BD56-104 Fab on BA.4/5 RBD
HCDR3 epitope
F490
T470
HCDR1
S31
L55
I54
L492
HCDR2
I52
I468
I57
L452R
HFR3
D59(FR3)
F60(FR3)
LCDR3
E62(FR3)
R346
HCDR2
HCDR1
HCDR3
LCDR1
LC epitope
R357
N26
LCDR1
HCDR2
HCDR1
HCDR3
Y351
I468
Y102
R466
LCDR3
N109
S103
E465
S107
G104

d

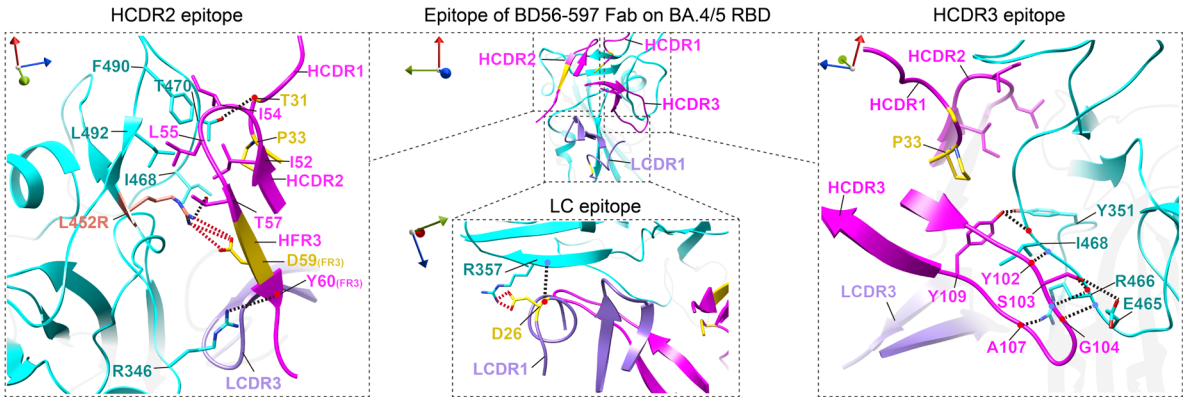
HCDR2 epitope
Epitope of BD56-597 Fab on BA.4/5 RBD
HCDR3 epitope
F490
T470
HCDR1
T31
I54
L492
L55
P33
I52
I468
HCDR2
L452R
T57
HFR3
D59(FR3)
Y60(FR3)
R346
LCDR3
HCDR2
HCDR1
HCDR3
LCDR1
LC epitope
R357
D26
LCDR1
HCDR2
HCDR1
P33
HCDR3
Y351
I468
Y102
R466
LCDR3
Y109
S103
E465
A107
G104

1163 **Fig. 3. Epitopes of C092, C807, BD56-104 and BD56-597 on BA.4/5 RBD.**

1164 **a-d**, HCDR2, HCDR3, and LC epitopes of C092 (**a**), C807 (**b**), BD56-104 (**c**), BD56-597 (**d**)
1165 are shown from rotated views. RBD, Fab-HC, and Fab-LC residues are colored in cyan,
1166 magenta, and purple, respectively. Antibody residues introduced by somatic hypermutation
1167 are colored in yellow, while residue L452R mutated in BA.4/5 RBD is colored in salmon.
1168 The backbone carbonyl oxygens and amide nitrogens are indicated by red and blue dots,
1169 respectively. Hydrogen bonds and salt bridges are shown as black and red dash lines,
1170 respectively.

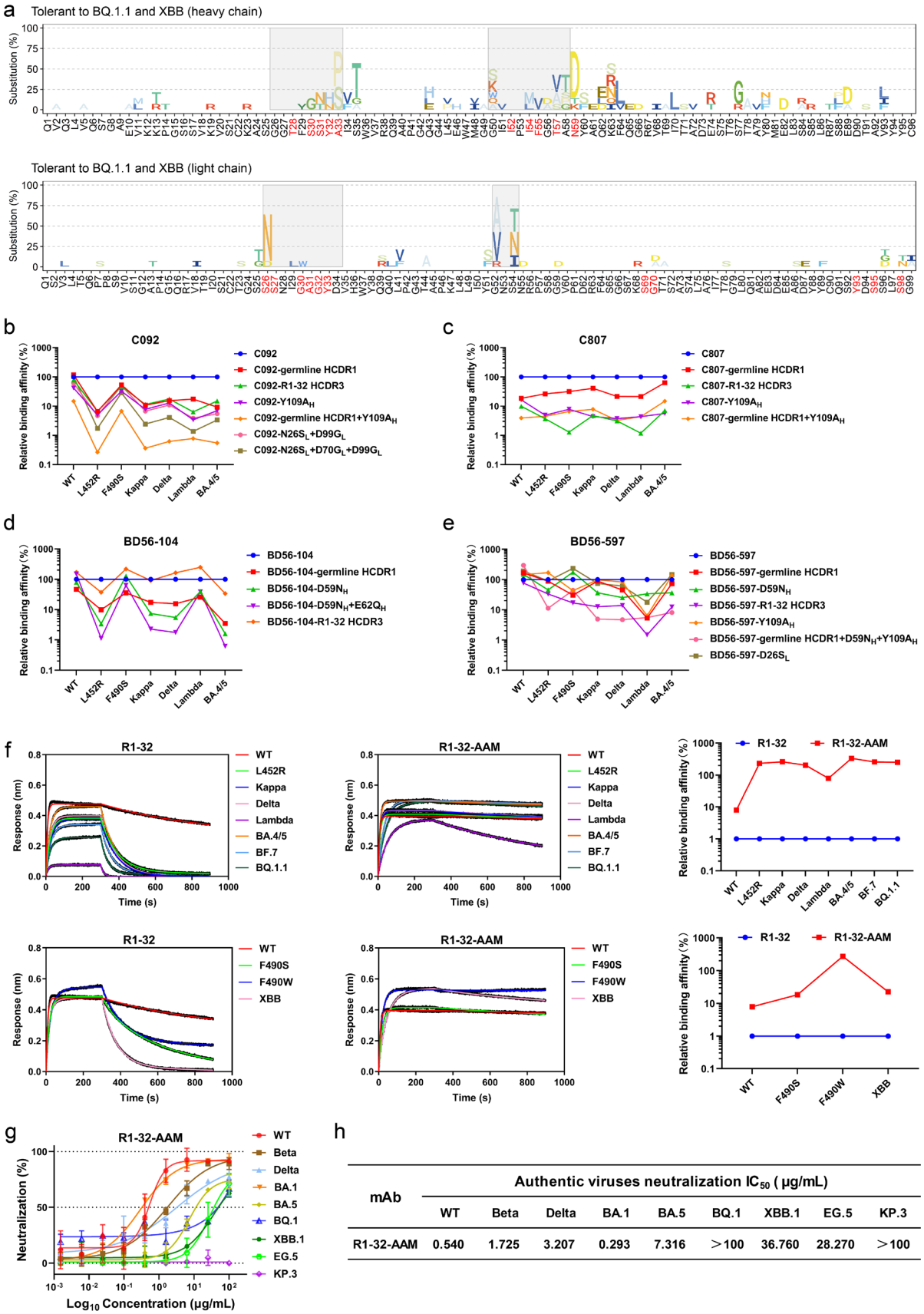

h

mAb	Authentic viruses neutralization IC_{50} (μg/mL)								
	WT	Beta	Delta	BA.1	BA.5	BQ.1	XBB.1	EG.5	KP.3
R1-32-AAM	0.540	1.725	3.207	0.293	7.316	>100	36.760	28.270	>100

1171

1172 **Fig. 4. Affinity maturation confers mutation tolerance to R1-32-like**
1173 **antibodies.**

1174 **a,** Frequency of somatic hypermutations (SHMs) in R1-32-like antibodies tolerant to BQ.1.1
1175 and XBB. The residues involved in epitope binding are colored in red. **b-e**, Relative binding
1176 affinities of antibody mutants derived from C092 (**b**), C807 (**c**), BD56-104 (**d**), and BD56-
1177 597 (**e**) to the RBDs of SARS-CoV-2 wild-type, L452R, F490S, Kappa, Delta, Lambda, and
1178 BA.4/5. The constructed C092 mutants include C092-germline HCDR1 (HCDR1 reverted to
1179 germline sequence), C092-R1-32 HCDR3 (HCDR3 replaced with R1-32 HCDR3), C092-
1180 $Y109A_H$, C092-germline HCDR1+$Y109A_H$, C092-$N26S_L$+$D99G_L$, and C092-
1181 $N26S_L$+$D70G_L$+$99G_L$. The C807 mutants include C807-germline HCDR1, C807-R1-32
1182 HCDR3, C807-$Y109A_H$, and C807-germline HCDR1+$Y109A_H$. The BD56-104 mutants
1183 include BD56-104 germline HCDR1, BD56-104-$D59N_H$, BD56-104+$D59N_H$+$E62Q_H$, and
1184 BD56-104-R1-32 HCDR3. The BD56-597 mutants include BD56-597-germline HCDR1,
1185 BD56-597-$D59N_H$, BD56-597-R1-32 HCDR3, BD56-597-$Y109A_H$, BD56-597-germline
1186 HCDR1-$D59N_H$+$Y109A_H$, BD56-597-$D26S_L$. Affinity changes of mutants are normalized to
1187 K_Ds of the corresponding unmodified antibody (set as 100%). Binding curves are shown in
1188 **Fig. S11a-d,** and K_D values used for comparisons are shown in **Table S3**. **f**, Binding curves
1189 of R1-32 and R1-32-AAM to the RBDs of wild-type, L452R, Kappa, Delta, Lambda, BA.4/5,
1190 BF.7, BQ.1.1, F490S, F490W, and XBB. Affinity changes of R1-32-AAM are normalized to
1191 K_Ds of R1-32 (set as 1%). K_D values used for comparisons are shown in **Table S4**. **g**,
1192 Neutralization activities of R1-32-AAM towards SARS-CoV-2 wild-type, Beta, Delta,
1193 Omicron BA.1, BA.5, BQ.1, XBB.1, EG.5, and KP.3 authentic viruses. Data are presented as
1194 mean ± SD (n = 2). IC_{50} values are summarized in **h**.

a

	type-1									type-2	type-3		
	SARS-CoV-2	Pangolin-CoV -GD-2019	Bat-CoV-RaTG13	Pangolin-CoV -GX-2017	Laos-20-52	Laos-20-236	Bat-CoV-RsSHC014	Bat-CoV-WIV1	SARS-CoV-1	BtKY72	GX2013	HeB2013	RmYN02
C092	0.046	0.111	0.177	0.262	0.059	0.034	0.622	21.3	no binding	29.2	26.3	34.9	31.5
C807	0.118	0.613	0.738	0.469	0.972	0.687	3.50	7.50	341	54.5	31.1	103	20.3
BD56-104	0.038	0.177	0.227	0.117	0.144	0.082	48.0	no binding	no binding	weak binding	weak binding	weak binding	weak binding
BD56-597	0.048	0.016	0.284	0.086	0.104	0.033	0.198	7.19	weak binding	223	159	weak binding	287
ZL525	0.295	0.040	0.020	0.104	0.362	0.810	0.447	7.54	63.1	18.0	3.89	14.1	2.63
R1-32	0.931	0.777	38.2	4.76	0.963	1.80	297	no binding	no binding	no binding	no binding	no binding	no binding

K_D (nM) < 1 | 1-100 | > 100 | no binding

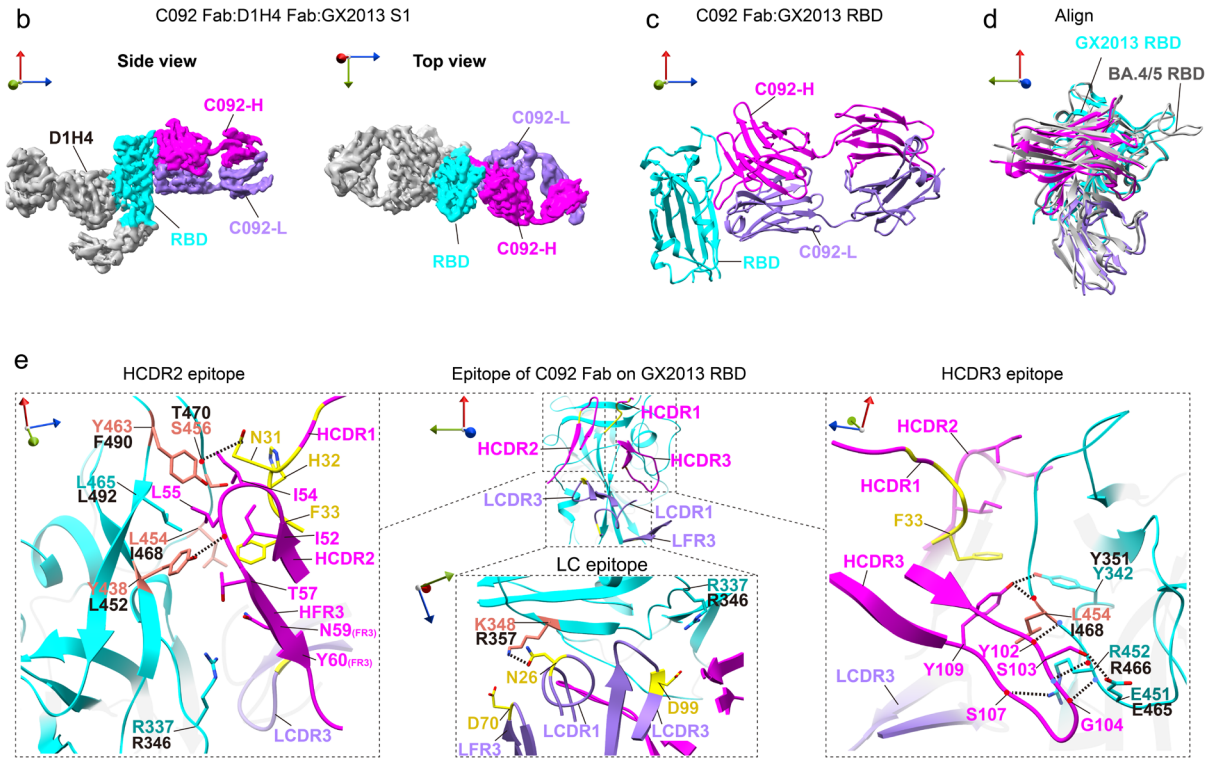

Fig. 5. Affinity maturation confers R1-32-like antibodies with broader SARSr- CoVs binding.

a, Binding affinities of R1-32-like antibodies to the RBDs of SARS-related coronaviruses (SARSr-CoVs). K_Ds (nM) are shown, with values <1, 1-100, >100 nM, and no binding colored in green, yellow, orange, and red, respectively. Binding curves and detailed kinetic parameters are provided in **Fig. S12 and Table S5**. **b**, Cryo-EM densities of the GX2013 S1:C092 Fab:D1H4 Fab complex. C092 Fab-HC, Fab-LC, and RBD are colored in magenta, purple, and cyan, respectively; the rest of the S1 and D1H4 Fab are colored grey. **c**, Structure of the GX2013 RBD:C092 Fab complex derived from the density in panel **b**. **d**, Comparison of C092 binding to GX2013 RBD and BA.4/5 RBD; the BA.4/5 RBD:C092 Fab complex is shown in grey. **e**, C092 HCDR2, HCDR3, and LC epitopes are shown from rotated views. Residues introduced by somatic hypermutation are colored in yellow, and epitope residues differing from SARS-CoV-2 wild-type RBD are colored in salmon. GX2013 RBD residues are labeled with the corresponding SARS-CoV-2 residues indicated in black. The backbone

carbonyl oxygens and amide nitrogens are indicated by red and blue dots, respectively, and hydrogen bonds are shown as black dash lines.

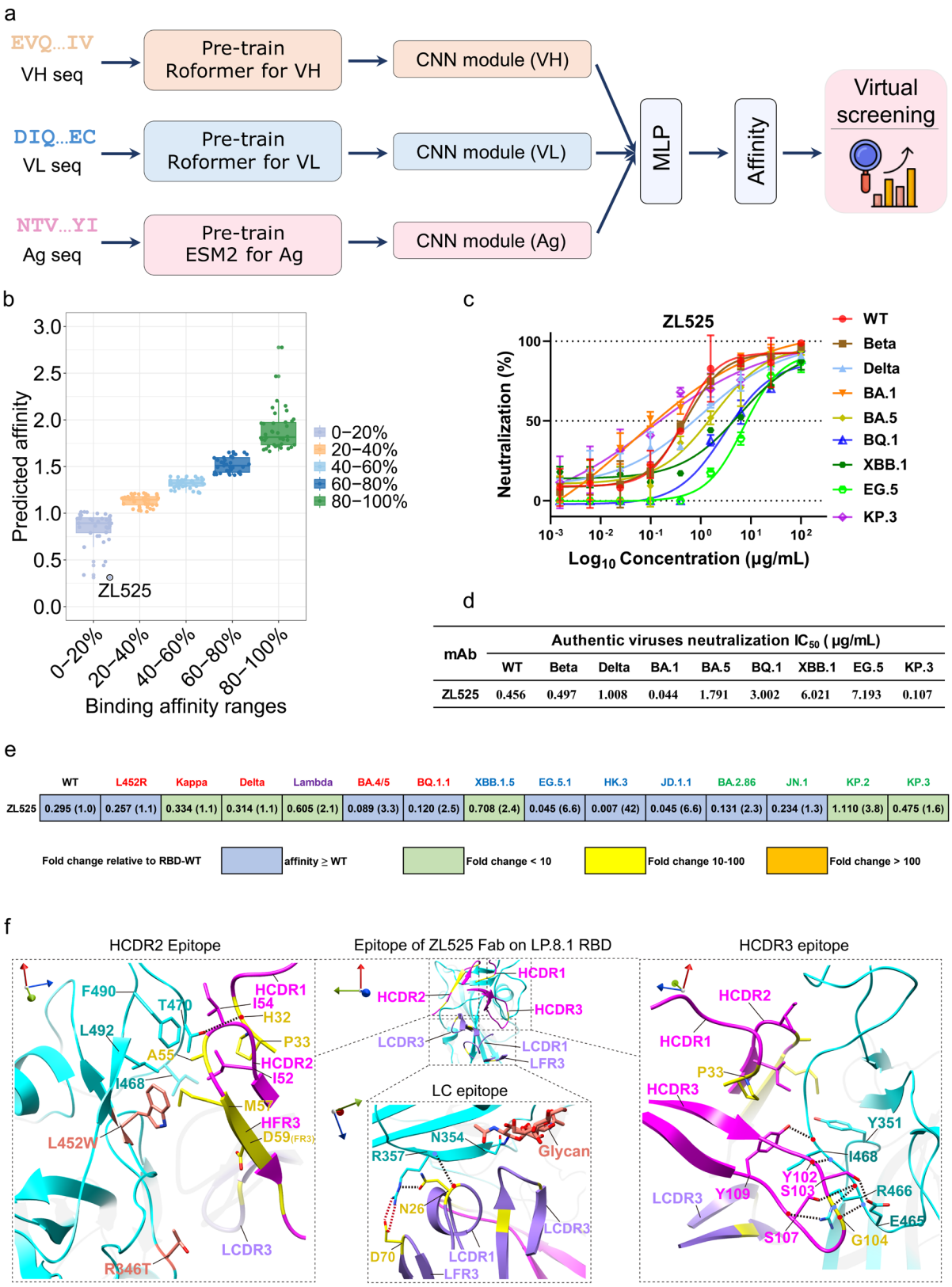

Fig. 6. AI-based discovery of an ultrapotent and broadly R1-32-like neutralizing antibody ZL525.

a, Workflow of the virtual screening pipeline based on pre-trained antibody language models. **b**, Distribution of predicted affinities of the 190 R1-32-like mAbs. **c**, Neutralization activities

1217 of the ZL525 towards SARS-CoV-2 wild-type, Beta, Delta, Omicron BA.1, BA.5, BQ.1,
1218 XBB.1, EG.5, and KP.3 authentic viruses. Data are shown as mean ± SD (n = 2). IC_{50} values
1219 are summarized in **d**. **e,** Binding affinities of ZL525 to RBDs carrying $L452_{SARS2}$ or
1220 $F490_{SARS2}$ substitutions and newly emerging variants. Dissociation constant K_Ds (nM) are
1221 shown, with fold changes relative to wild-type RBD indicated in parentheses. Binding
1222 affinities higher than the wild-type RBD are shown in blue, whereas reduced affinities (<10-
1223 fold, 10-100-fold, and >100-fold relative to wild-type) are shown in green, yellow, and
1224 orange, respectively. RBDs carrying L452, F490, or both substitutions are colored in red,
1225 blue, and purple, respectively. RBDs carrying L452 substitution together with N354
1226 glycosylation are colored in green. Binding assays were performed by BLI, and detailed
1227 kinetic parameters are provided in **Table S8. f**, ZL525 HCDR2, HCDR3, and LC epitopes are
1228 shown from rotated views. Antibody residues introduced by somatic hypermutation are
1229 colored in yellow, and residues $L452W_{SARS2}$ and $R346T_{SARS2}$ mutated in the LP.8.1 RBD are
1230 colored in salmon. The backbone carbonyl oxygens and amide nitrogens are indicated by red
1231 and blue dots, respectively. Hydrogen bonds and salt bridges are shown as black and red dash
1232 lines, respectively.